LETTER

Heterointerface effects in the electrointercalation of van der Waals heterostructures

D. Kwabena Bediako[1,6], Mehdi Rezaee[2,3,6], Hyobin Yoo[1], Daniel T. Larson[1], S. Y. Frank Zhao[1], Takashi Taniguchi[4], Kenji Watanabe[4], Tina L. Brower-Thomas[5], Efthimios Kaxiras[1,3] & Philip Kim[1,3]*

Molecular-scale manipulation of electronic and ionic charge accumulation in materials is the backbone of electrochemical energy storage[1–4]. Layered van der Waals (vdW) crystals are a diverse family of materials into which mobile ions can electrochemically intercalate into the interlamellar gaps of the host atomic lattice[5,6]. The structural diversity of such materials enables the interfacial properties of composites to be optimized to improve ion intercalation for energy storage and electronic devices[7–12]. However, the ability of heterolayers to modify intercalation reactions, and their role at the atomic level, are yet to be elucidated. Here we demonstrate the electrointercalation of lithium at the level of individual atomic interfaces of dissimilar vdW layers. Electrochemical devices based on vdW heterostructures[13] of stacked hexagonal boron nitride, graphene and molybdenum dichalcogenide (MoX_2; X = S, Se) layers are constructed. We use transmission electron microscopy, in situ magnetoresistance and optical spectroscopy techniques, as well as low-temperature quantum magneto-oscillation measurements and ab initio calculations, to resolve the intermediate stages of lithium intercalation at heterointerfaces. The formation of vdW heterointerfaces between graphene and MoX_2 results in a more than tenfold greater accumulation of charge in MoX_2 when compared to MoX_2/MoX_2 homointerfaces, while enforcing a more negative intercalation potential than that of bulk MoX_2 by at least 0.5 V. Beyond energy storage, our combined experimental and computational methodology for manipulating and characterizing the electrochemical behaviour of layered systems opens new pathways to control the charge density in two-dimensional electronic and optoelectronic devices.

To examine the role of the vdW heterointerface in intercalation, we assembled layers of graphene, molybdenum dichalcogenides (MoX_2, X = S, Se) and hexagonal boron nitride (h-BN) into various precise arrangements. Figure 1a shows a series of five different heterostructures (structures I to V) created using vdW assembly[14]. Structure I is a simple vdW structure of graphene encapsulated by h-BN; this structure was the subject of our previous studies[15] and serves as a reference point in the present study. Structures II–V are combinations of atomically thin single crystals of graphene and MoX_2 encapsulated by h-BN, with several vdW heterointerfaces between atomic layers. The etched boundaries of the vdW stacks are exposed to the electrolyte. These electrochemical device architectures were investigated as the working electrodes of on-chip microelectrochemical cells, as shown in Fig. 1b, c. Using the recently developed Hall potentiometry method (see Methods), we can extract both the longitudinal resistance, R_{xx}, of the heterostructure working electrode as well as the Hall carrier density, n_H, while the reaction driving force (potential, E) is altered[15]. As such, the progress of the electrochemical reaction can be precisely monitored in this mesoscopic system.

Figure 2 presents an exemplary set of results for electrointercalation of a heterostructure stack of structure II (h-BN/MoS_2/graphene/h-BN). From the behaviour of R_{xx} and n_H as a function of E, four distinct phases (phase 1–4) can be distinguished in the electrochemical reaction. This in situ monitoring of R_{xx} and n_H provides more direct information regarding the stages of intercalation than do the traditional electrochemical approaches because it is insensitive to extraneous interfacial reactions (see Extended Data Fig. 1 for a comparison). The transport features in phase 1 (for $E > -2.3$ V) replicate the purely electrostatic doping behaviour observed in electric double-layer gating of graphene[16]. With increasingly negative E, several intercalation processes occur, as evidenced by pronounced jumps in R_{xx} and n_H. The latter features in phases 3 and 4, specifically the peak in R_{xx} that occurs together with the surge in n_H, are key signatures of ion intercalation involving a high-mobility graphene layer[15]. The intercalation process results in a decline in electron mobility, as Li^+ ions become closely associated with the graphene lattice and act as scattering sites for mobile electrons[17]. Ultimately, the resistance decreases as mounting carrier densities supersede this sudden decrease in mobility[15]. Deintercalation by sweeping E towards a potential of 0 V reverses doping and recovers R_{xx} and n_H to values similar to those of the pristine heterostructure (Extended Data Fig. 1a). The total carrier densities for intercalated structure-II stacks approach $n_H = 2 \times 10^{14}$ cm^{-2} (Extended Data Fig. 2), which is between three and ten times the maximal densities observed[15] for intercalated structure I (($2–7) \times 10^{13}$ cm^{-2}).

Insight into the participation of MoX_2 in this electrochemical reaction was provided by operando photoluminescence and Raman spectroelectrochemistry. In Fig. 2b, photoluminescence data reveal distinct changes in the optical profile of the semiconducting 1H-MoS_2 layer. Specifically, we found that the photoluminescence peak that is consistent with the formation of negatively charged trions (A^-)[18] appears at the later stage of the intercalation process ($E < -3$ V), which indicates that a strongly electron-doped 1H-MoS_2 phase persists immediately before the main intercalation stage. Beyond this point the photoluminescence is fully quenched, and Raman spectral features of the MoS_2 (and graphene) layer are lost owing to Pauli blocking[15,19,20] (Extended Data Fig. 3a). Deintercalation recovered the original Raman signatures of graphene, and revealed a reduced spectral intensity of the E_{2g}^1 and A_{1g} modes of MoS_2 as well as the emergence of a series of weak peaks between around 150 cm^{-1} and 230 cm^{-1} (Fig. 2c). These results are consistent with an intercalation-induced phase transition from the semiconducting H-MoS_2 phase to a metallic T phase with an additional lattice distortion (denoted as T′)[21,22]. The low-wavenumber Raman features are characteristic of the so-called 'J' modes of T-MoS_2 and T′-MoS_2[21,23–25]. Figure 2d–g and Extended Data Fig. 3c–g show the corresponding photoluminescence and Raman spectra homogeneously distributed across the interfacial areas, indicating homogeneity of the intercalation–deintercalation processes.

Low-temperature magnetotransport studies in the intercalated vdW heterostructure devices provide a new route to investigate the distribution of charge on each two-dimensional layer after intercalation. For an intercalated structure-II device, Fig. 3a shows that the Hall resistance, R_{xy}, is linear in magnetic field B, from which we estimate n_H to be

[1]Department of Physics, Harvard University, Cambridge, MA, USA. [2]Department of Electrical Engineering, Howard University, Washington, DC, USA. [3]School of Engineering and Applied Sciences, Harvard University, Cambridge, MA, USA. [4]National Institute for Materials Science, Tsukuba, Japan. [5]Department of Chemical Engineering, Howard University, Washington, DC, USA. [6]These authors contributed equally: D. Kwabena Bediako, Mehdi Rezaee *e-mail: pkim@physics.harvard.edu
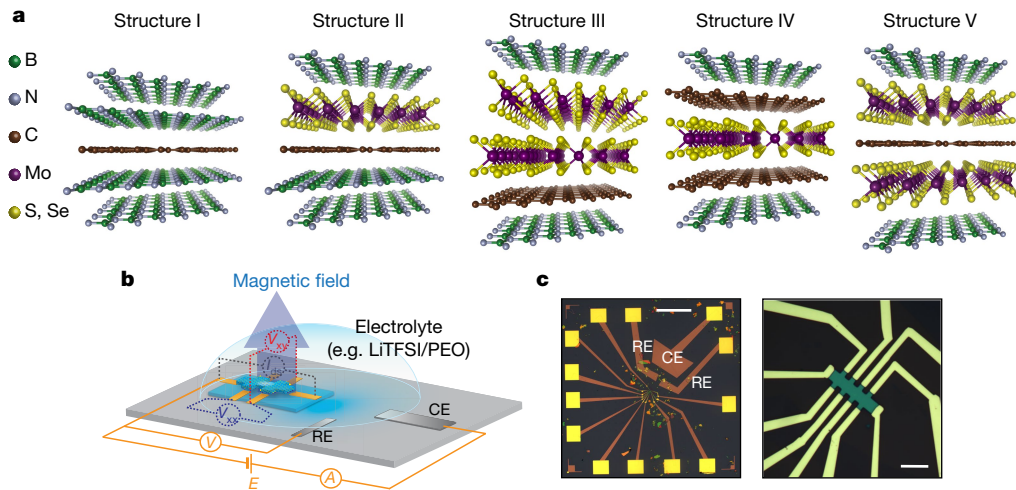
Fig. 1 | Van der Waals heterostructures for lithium intercalation.
a, Atomic models of the heterostructure series used for investigating the effects of heterolayers on intercalation capacities and thermodynamics. **b**, Schematic of the mesoscopic electrochemical cell. **c**, Optical micrographs of an on-chip electrochemical cell for charge transport and optical measurements during electrointercalation. Scale bars, left, 500 μm; right, 10 μm. CE, counter electrode; RE, reference electrode.

1.0×10^{14} cm^{-2}. The magnetoresistance, $R_{xx}(B)$, exhibits a pronounced peak near $B = 0$, which is presumably related to the weak localization behaviour owing to intervalley scattering of intercalated Li$^+$ ions[17]. We observe well-defined Shubnikov–de Haas (SdH) oscillations[26,27] when $B > 3$ T, which indicates both homogeneity of the lithium-intercalated heterostructure and a high-quality two-dimensional electron gas (2DEG) with an associated carrier density of 2×10^{13} cm^{-2} (see Methods). The discrepancy between n_{SdH} and n_H is in stark contrast with those observed for structure I (Extended Data Fig. 4), and is consistent with a two-channel electronic system, in which a higher-mobility 2DEG produces SdH oscillations corresponding to a lower-density $n_{SdH} < n_H$, while another channel contains the vast majority of electron density ($n_H - n_{SdH}$) with a lower mobility.

The decrease in amplitude of the SdH oscillation with increasing temperature (Fig. 3b) reveals an effective mass (m^*) of electrons equal to $0.11m_0$ (m_0 is the electron rest mass), close to the value of $0.099m_0$ that we obtain for intercalated structure I (h-BN/graphene/h-BN)

doped to a density of approximately 2×10^{13} cm^{-2} in graphene (additional transport quantities are summarized in Extended Data Table 1). From the Landau fan diagram of structure II (Fig. 3c) we observe that the SdH quantum oscillations are strongly dependent on the voltage applied to the silicon backgate, V_g, pointing to the graphene as the origin of the magneto-oscillations (see Methods). Correspondingly, we find that n_{SdH} and n_H exhibit the same dependence on V_g (Fig. 3d), consistent with the bottom graphene layer (around 10^{13} electrons per cm^2) serving to shield the overlying MoS$_2$ sheet (around 10^{14} electrons per cm^2) from the electrostatic influence of V_g. In this case, the dependence of the total density, given by n_H, simply follows the dependence of one of its components n_{SdH}.

Having established that the carrier density distribution on these heterostructures lies strongly on the metal dichalcogenide layer, it is notable that intercalation into structure-III stacks (in which $n_H = (1.4$–$1.9) \times 10^{14}$ cm^{-2}, see Extended Data Fig. 5) does not lead to carrier densities in excess of those seen in typical structure-II samples.
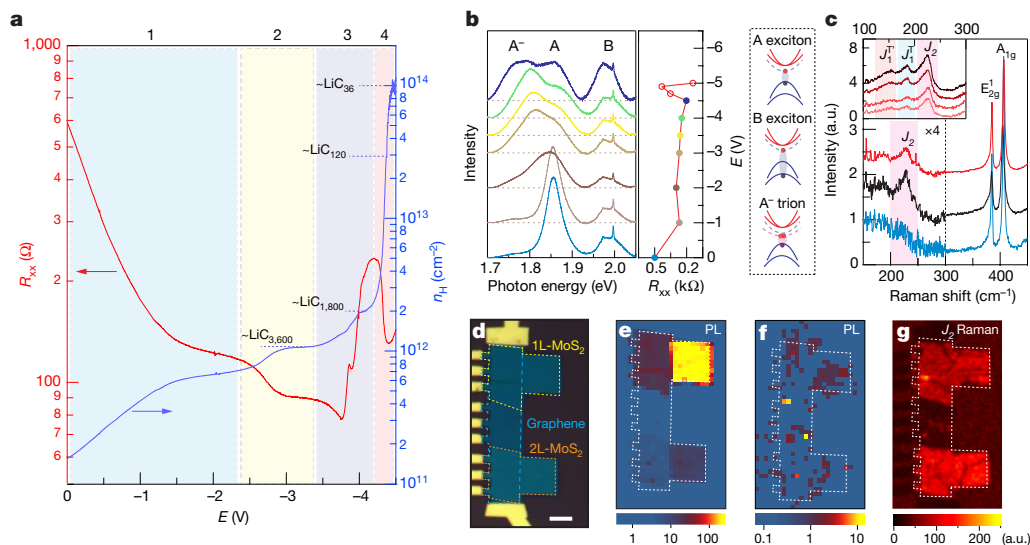

Fig. 2 | Intercalation of structure-II devices. a, Hall potentiogram recorded at 325 K for a graphene/MoSe$_2$ device ($B = 0.5$ T). **b**, Operando photoluminescence (left) and resistance (middle) measurements for graphene/MoS$_2$ at 325 K, with schematic representations of the exciton quasiparticles (right). **c**, Ex situ Raman spectra of a pristine (bottom), cycled (middle) and subsequently annealed (top) heterostructure. Inset, Raman spectra after annealing of (from bottom to top) MoS$_2$, graphene/MoS$_2$, 2L-MoS$_2$ and graphene/2L-MoS$_2$. **d**, Optical micrograph of the device used in spectroscopic mapping. Scale bar, 5 μm. **e**–**g**, Ex situ photoluminescence (**e**, **f**) and 200–250 cm^{-1} Raman (**g**) spatial maps of the device in **d** before intercalation (**e**) after one cycle (**f**) and after subsequent annealing (**g**).
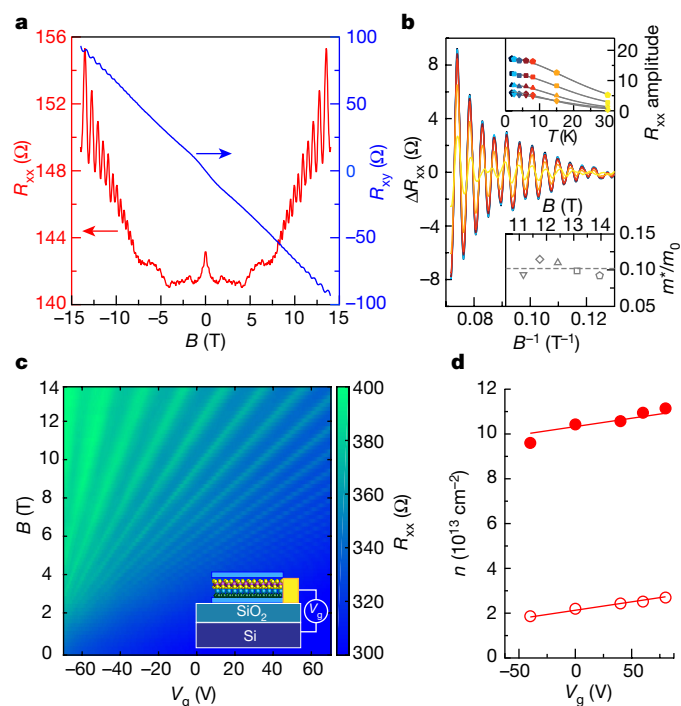
Fig. 3 | Quantum transport. a, Four-terminal R_{xx} and R_{xy} as a function of perpendicular B for intercalated structure II. **b**, Temperature dependence of SdH oscillations. Top inset, SdH amplitude as a function of T at five values of B. The solid lines depict fits according to the Lifshitz–Kosevich formalism. Bottom inset, effective masses m^* extracted from fits (m_0, free electron mass). **c**, Landau fan diagram of R_{xx} (V_g, B) after intercalation. Inset, schematic of the intercalated heterostructure used with the graphene layer beneath MoS$_2$. **d**, Dependence of n_{SdH} (open circles) and n_{Hall} (filled circles) on V_g. Lines represent fits assuming a Si backgate capacitance of 1.2×10^{-8} F cm^{-2}.
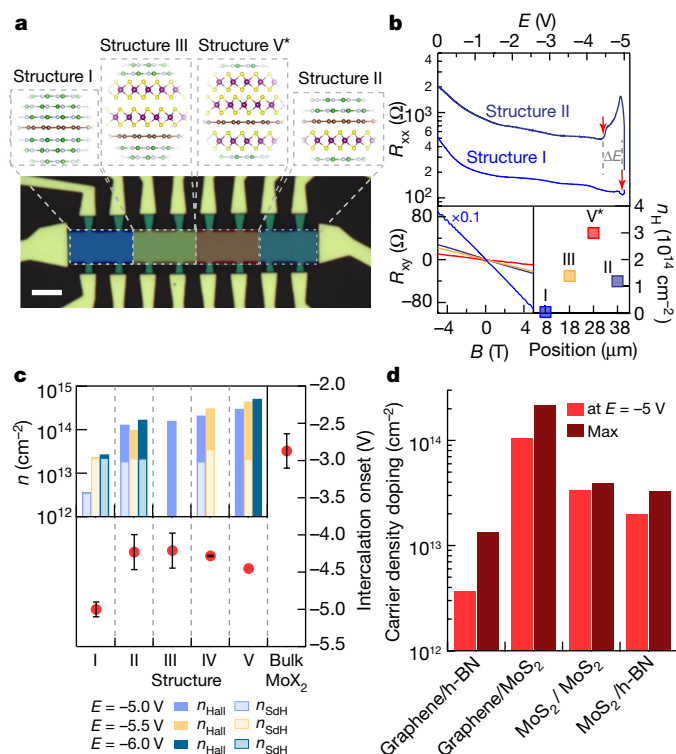

Fig. 4 | Tuning intercalation with van der Waals heterolayers. a, Optical micrograph (false colour) of a device consisting of several heterostructure types (depicted in the associated illustration) arrayed along a graphene monolayer. Scale bar, 5 μm. **b**, Top, R_{xx} during electrochemical gating of two regions of the device in **a**. Bottom left, Hall data following polarization of the device in **a** to −5.0 V. Bottom right, n_H from each region of the device. **c**, Intercalation onset potentials of vdW heterostructures and bulk MoX$_2$ (see also Extended Data Fig. 9a). Error bars, where present, represent the standard deviation (from left to right, $n = 3, 6, 4, 2, 1, 3$) of measurements from multiple devices and/or distinct contact pairs. Inset, mean charge densities after intercalation. n_H, indicative of the total density, is depicted by the overall bar height, and graphene partial densities from SdH data (where available) are indicated by the lighter sub-bars. **d**, Estimated doping level of vdW interfaces.

This suggests that it is the graphene/MoX$_2$ heterointerface that contains the vast majority of intercalated ions, rather than the h-BN/MoX$_2$ or MoX$_2$/MoX$_2$ interfaces. To investigate this further, we created heteroarchitectures in which we designed in-plane variations of the structure type along a single graphene monolayer, as depicted in Fig. 4a. Simultaneous measurement of the transport characteristics at different lateral sections of the heterostructure devices during electrochemical polarization (Fig. 4b, Extended Data Figs. 6, 7) revealed that the onset of intercalation into graphene/MoX$_2$ takes place at about $\Delta E^o = +0.5$ to $+0.75$ V versus that of graphene/h-BN. Notwithstanding the considerably negative potential, it is noteworthy that the dichalcogenides in these graphene/MoX$_2$ heterostructures are not decomposed to lithium polychalcogenides as occurs in the bulk[20] (Extended Data Fig. 8), which indicates a widened window of electrochemical stability. This enhanced stability may be a result of dimensional confinement that restricts polysulfide/Mo^0 nucleation and product diffusion[12]. Hall resistance measurements at specific regions of the device (Fig. 4b, bottom left) unequivocally demonstrate the critical role of direct graphene/MoX$_2$ heterointerfaces in markedly enhancing the carrier and charge capacities in vdW heterostructure electrodes. We found that encapsulating a graphene monolayer between layers of MoX$_2$ (as in structures V and V*), thereby creating two graphene/dichalcogenide heterointerfaces, produced intercalation capacities that were more than double those of the 'isomeric' structure-III region within the same device (Fig. 4b, bottom right). The intercalation onset potentials of the different structures (Fig. 4c and Extended Data Fig. 9a) emphasize that graphene/MoX$_2$ interfaces have the dominant effect on the intercalation properties; the onset of intercalation is effectively identical across structures II to V, and lies distinctly between those of structure I and bulk MoX$_2$. Capacities as high as 6.2×10^{14} cm^{-2} (Fig. 4c, inset and Extended Data Fig. 9b, c) are attainable in structure-V devices. However, in all these structures,

the graphene density (n_{SdH}) exhibits a maximum value of around 2×10^{13} cm^{-2}, which is indicative of a strong preference for charge transfer to the dichalcogenide layers (n is approximately 3×10^{14} cm^{-2} per MoX$_2$ layer). Assuming additive Li$^+$-ion capacities, we can estimate the electrochemically accessible capacity of each vdW interface as plotted in Fig. 4d, which shows that the capacity of the graphene/MoS$_2$ interface is more than ten times that of the other interfaces. These results highlight the importance of the graphene heterolayer in enhancing electrochemical charge accumulation in MoX$_2$ while also directing intercalation at a more negative voltage than that of bulk MoX$_2$.

Finally, we explored the atomic-scale structural evolution of these layers using ex situ scanning transmission electron microscopy (STEM). As expected, data from the pristine heterostructure were fully consistent with that of H-MoS$_2$ (Fig. 5b). The onset of intercalation resulted in an increasingly disordered MoS$_2$ lattice, as evidenced by the progressive splitting of the MoS$_2$ Bragg spots in selected area electron diffraction (SAED) patterns. Importantly, we observed this signature of disorder at the edges of the heterostructure even before the peak in R_{xx}, while the interior remained pristine (Extended Data Fig. 10). Full intercalation resulted in the observation of a ring in the SAED data (Fig. 5c, inset). Notably, aberration-corrected STEM imaging (Fig. 5c and Extended Data Fig. 11) uncovered crystalline order within domains of approximately 5–10 nm in size (Fig. 5c, right and Extended Data Fig. 11). We also observed distinct voids of around 1 nm in size in the metal dichalcogenide layer, similar to the findings of TEM studies
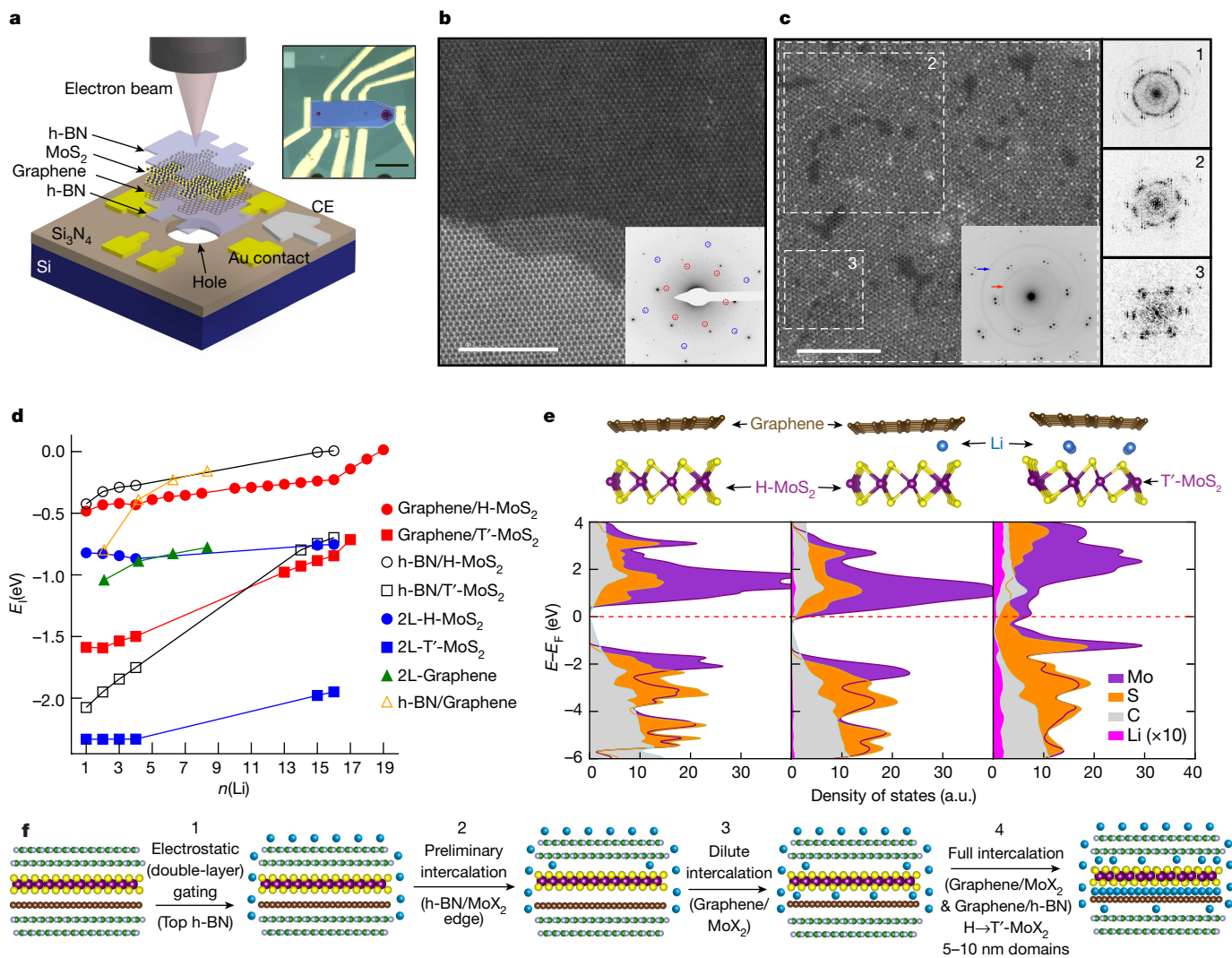
Fig. 5 | Structural evolution of van de Waals heterostructures with intercalation. a, Schematic of vdW heterostructure device for (S)TEM analysis. Inset, optical micrograph of a representative device. Scale bar, 10 µm. **b**, **c**, High-angle annular dark-field (HAADF) STEM images of structure-II devices before intercalation (**b**) and after one cycle (**c**). Scale bars, 5 nm. Insets, the corresponding SAED patterns. Diffraction features originating from $\{10\bar{1}0\}$ and $\{11\bar{2}0\}$ planes of MoS_2 are marked with red and blue circles or arrows, respectively. In **c**, fast Fourier transforms obtained from the regions indicated with the dashed boxes are shown on the right. **d**, Computed lithium-atom binding energy as a function of the number of lithium atoms in the supercell (see Methods). 2L-graphene and h-BN/graphene data are adapted from ref. [28]. **e**, Computed relaxed structures (top) and density-of-states plots (bottom) for pristine (left), and lithium-intercalated (middle, 1 Li; right, 4 Li) heterostructures. **f**, Proposed mechanism of vdW heterostructure intercalation.

of chemically (^{n}BuLi)-lithiated and exfoliated MoS_2[22]. This structural disruption is probably caused by the strain introduced into the MoX_2 layer during lithiation and the associated progression of the H- to T′ phase transformation along the lattice. Despite these structural defects, the resulting basal-plane charge transport in MoS_2 layers is reasonably high (as shown in Extended Data Table 1), which indicates that the intercalation–deintercalation process leaves the MoS_2 structure largely intact and as an electrically contiguous layer.

The tuning of intercalation potentials using vdW heterostructures is well explained by the modification of theoretical lithium binding energetics, as observed in density functional theory (DFT) calculations (Fig. 5d). First, these calculations reveal that the T′-MoS_2 phase has a considerably stronger binding affinity for lithium atoms than does H-MoS_2. As such, a local phase transformation upon doping should lead to a cooperative effect, by which it becomes increasingly favourable to intercalate lithium into that local vdW region as the dichalcogenide undergoes the semiconductor (H) to metallic (T′) transformation, thereby lowering the activation barrier for Li^+ insertion. This phase transition is manifested by the closing of the band gap, and the Fermi level crosses a band with large density of states, as shown in Fig. 5e

and Extended Data Fig. 12. Furthermore, since h-BN is an inert, wide-gap insulator and is non-redox-active, the energetics of initial lithium intercalation are only slightly perturbed in the case of h-BN/T′-MoS_2 compared to T′-MoS_2/T′-MoS_2. By contrast, graphene heterolayers have a substantially stronger attenuating effect on the binding energy of lithium, yet still the reaction is more exergonic than that of lithium with h-BN/graphene or graphene/graphene[28] (Fig. 5d). As a result, we observe a positive shift in intercalation potential for the graphene/MoS_2 heterolayer compared to h-BN/graphene in Fig. 4b, c.

Taken together, our experimental results are consistent with the electrochemical reaction scheme presented in Fig. 5f. This mechanism involves charge transfer to both graphene and MoX_2 in the initial stages of the electrochemical gating process. Dilute concentrations of Li^+ ions are intercalated at modest potentials into MoX_2/h-BN (and MoX_2/ MoX_2) heterointerfaces. However, on the basis of SAED data of our heterostructures and previous observations of slow chemical lithiation of bulk MoS_2[20], Li^+ ion intercalants of these interfaces appear most concentrated proximate to the heterostructure/electrolyte interface (where the electric field is strongest and some T′-MoS_2 can be formed locally from electrostatic double-layer gating). The graphene/MoX_2

interface possesses a unique intercalation potential that is more positive than that of graphene/h-BN, and as such this is the next interface to undergo intercalation. The exceptional electronic mobility of graphene (sufficient to display quantum oscillations even after interfacial ion intercalation) provides a lower-resistance electronic pathway—despite a lower partial carrier density—which enables its immediate interface with the MoX_2 layer to undergo ionic doping more efficiently than the adjacent MoX_2/MoX_2 homointerfaces. Eventually a highly doped, two-dimensional nanocrystalline T'-MoX_2 is formed upon complete intercalation of the graphene/dichalcogenide heterostructure.

We note that typically, in battery electrodes consisting of layered-material composites, carbonaceous additives such as graphene serve primarily to improve cyclability, particularly over the course of additional conversion reactions that can form insulating and structurally expanded conversion phases[7,8,10,11]. These approaches do not seek to create or exploit a direct vdW contact between individual atomic layers as a means of tuning the intercalation reaction itself. Our observations of lithium-ion intercalation at individual atomic interfaces motivate the use of vdW heteroepitaxy as a promising strategy to realize new engineered functional interfaces for energy conversion and storage by manipulating the ion storage modes and 'job-sharing'[4] characteristics of hybrid electrodes. Furthermore, our demonstrated control over intercalation energetics, the resultant spatial carrier-density profile, and the realization of ultra-high charge densities using vdW heterointerfaces opens new possibilities for two-dimensional plasmonic device schemes[29] that would require large variations in charge density.

Online content

Any Methods, including any statements of data availability and Nature Research reporting summaries, along with any additional references and Source Data files, are available in the online version of the paper at https://doi.org/10.1038/s41586-018-0205-0.

1. Armand, M. & Tarascon, J.-M. Building better batteries. *Nature* **451**, 652–657 (2008).
2. Goodenough, J. B. & Park, K.-S. The Li-ion rechargeable battery: a perspective. *J. Am. Chem. Soc.* **135**, 1167–1176 (2013).
3. Simon, P., Gogotsi, Y. & Dunn, B. Materials science. Where do batteries end and supercapacitors begin? *Science* **343**, 1210–1211 (2014).
4. Maier, J. Thermodynamics of electrochemical lithium storage. *Angew. Chem. Int. Ed.* **52**, 4998–5026 (2013).
5. Ubbelohde, A. R. in *Intercalated Layered Materials* (ed. Lévy, F.A.) 1–32 (Riedel, Dordrecht, 1979).
6. Whittingham, M. S. Electrical energy storage and intercalation chemistry. *Science* **192**, 1126–1127 (1976).
7. Pomerantseva, E. & Gogotsi, Y. Two-dimensional heterostructures for energy storage. *Nat. Energy* **2**, 17089 (2017).
8. Chhowalla, M. et al. The chemistry of two-dimensional layered transition metal dichalcogenide nanosheets. *Nat. Chem.* **5**, 263–275 (2013).
9. Nitta, N., Wu, F., Lee, J. T. & Yushin, G. Li-ion battery materials: present and future. *Mater. Today* **18**, 252–264 (2015).
10. Sun, J. et al. A phosphorene-graphene hybrid material as a high-capacity anode for sodium-ion batteries. *Nat. Nanotechnol.* **10**, 980–985 (2015).
11. Oakes, L. et al. Interface strain in vertically stacked two-dimensional heterostructured carbon–MoS₂ nanosheets controls electrochemical reactivity. *Nat. Commun.* **7**, 11796 (2016).
12. Zhu, C., Mu, X., van Aken, P. A., Yu, Y. & Maier, J. Single-layered ultrasmall nanoplates of MoS₂ embedded in carbon nanofibers with excellent electrochemical performance for lithium and sodium storage. *Angew. Chem. Int. Ed.* **53**, 2152–2156 (2014).
13. Geim, A. K. & Grigorieva, I. V. Van der Waals heterostructures. *Nature* **499**, 419–425 (2013).
14. Wang, L. et al. One-dimensional electrical contact to a two-dimensional material. *Science* **342**, 614–617 (2013).
15. Zhao, S. Y. F. et al. Controlled electrochemical intercalation graphene/h-BN van der Waals heterostructures. *Nano Lett.* **18**, 460–466 (2018).
16. Das, A. et al. Monitoring dopants by Raman scattering in an electrochemically top-gated graphene transistor. *Nat. Nanotechnol.* **3**, 210–215 (2008).
17. Kühne, M. et al. Ultrafast lithium diffusion in bilayer graphene. *Nat. Nanotechnol.* **12**, 895–900 (2017).
18. Mak, K. F. et al. Tightly bound trions in monolayer MoS₂. *Nat. Mater.* **12**, 207–211 (2013).
19. Malard, L. M., Pimenta, M. A., Dresselhaus, G. & Dresselhaus, M. S. Raman spectroscopy in graphene. *Phys. Rep.* **473**, 51–87 (2009).
20. Xiong, F. et al. Li intercalation in MoS₂: in situ observation of its dynamics and tuning optical and electrical properties. *Nano Lett.* **15**, 6777–6784 (2015).
21. Eda, G. et al. Photoluminescence from chemically exfoliated MoS₂. *Nano Lett.* **11**, 5111–5116 (2011).
22. Eda, G. et al. Coherent atomic and electronic heterostructures of single-layer MoS₂. *ACS Nano* **6**, 7311–7317 (2012).
23. Yin, X. et al. Tunable inverted gap in monolayer quasi-metallic MoS₂ induced by strong charge–lattice coupling. *Nat. Commun.* **8**, 486 (2017).
24. Fan, X. et al. Fast and efficient preparation of exfoliated 2H MoS₂ nanosheets by sonication-assisted lithium intercalation and infrared laser-induced 1T to 2H phase reversion. *Nano Lett.* **15**, 5956–5960 (2015).
25. Singh, A. & Waghmare, U. V. in *2D Inorganic Materials Beyond Graphene* (eds Rao, C. N. R. & Waghmare, U. V.) 429–431 (World Scientific, New Jersey, 2017).
26. Shoenberg, D. *Magnetic Oscillation in Metals* (Cambridge Univ. Press, Cambridge, 1984).
27. Cao, H. et al. Quantized Hall effect and Shubnikov–de Haas oscillations in highly doped Bi₂Se₃: evidence for layered transport of bulk carriers. *Phys. Rev. Lett.* **108**, 216803 (2012).
28. Shirodkar, S. & Kaxiras, E. Li intercalation at graphene/hexagonal boron nitride interfaces. *Phys. Rev. B* **93**, 245438 (2016).
29. Shirodkar, S. N. et al. Visible quantum plasmons in highly-doped few-layer graphene. Preprint at https://arxiv.org/pdf/1703.01558v1 (2017).

Author contributions D.K.B., M.R. and H.Y. performed the experiments and analysed the data. D.K.B., S.Y.F.Z. and P.K. conceived the experiment. D.T.L. and E.K. performed the theoretical computations. K.W. and T.T. provided bulk h-BN crystals. D.K.B., M.R. and P.K. wrote the manuscript. All authors contributed to the overall scientific interpretation and edited the manuscript.

METHODS

Sample fabrication. Samples were fabricated in a similar way to that described in previous work[30,31]. In brief, mechanical exfoliation of Kish graphite (Covalent Materials Corp.) and molybdenum dichalcogenides, MoX_2 (X = S, Se) (HQ Graphene), onto p-doped silicon with 285 nm SiO_2 furnished crystals of the desired thickness, which were identified by optical contrast. Hexagonal boron nitride (h-BN) flakes of thickness 15–30 nm were similarly exfoliated and used to pick up graphene and/or MoX_2 layers in the designated order. Finally, release of these stacks onto a second flake of h-BN resulted in h-BN-encapsulated heterostructures that were subjected to annealing in high vacuum for 30 min at 350 °C. For the devices fabricated on silicon nitride membranes, thinner h-BN flakes ($\leq$5 nm) were used. Standard electron-beam lithography followed by evaporation of Cr/Pt (1 nm/9 nm) electrodes was used to define on-chip counter and pseudo-reference electrodes. Reactive ion etching (RIE) using a mixture of CHF_3, Ar, and O_2 was subsequently used to shape the heterostructure into a Hall bar. Another round of lithography was used to delineate an etch mask that overlaps with the protruding legs of the Hall bar. Immediately following another RIE step, the same etch mask was used as the metal deposition mask with Cr/Pd/Au (5 nm/15 nm/70 nm) contacts. This resulted in a one-dimensional edge-contact to the active layers and low contact resistances.

Electrochemical doping and intercalation. In an argon-filled glove box, 3.7 ml of anhydrous acetonitrile (dried with 3 Å molecular sieves; Sigma-Aldrich) was added to 0.3 g of polyethylene oxide (PEO; Sigma-Aldrich) and 50 mg of lithium bis(trifluoromethanesulfonyl)imide (LiTFSI). After stirring overnight, a 10–15 μl droplet of this electrolyte solution was cast onto the Si chip possessing the electrically contacted heterostructure stack, such that the droplet encompassed both the stack and the counter/reference electrodes. Rapid evaporation of the acetonitrile solvent yielded a solid polymer electrolyte for electrochemical studies. Additional extraneous solvent was removed by vacuum-drying the electrolyte overnight. Immediately before measurements the measurement device was isolated from ambient moisture and oxygen using a glass coverslip affixed to the chip carrier with vacuum grease. The device was then removed from the glove box and transferred promptly to the cryostat and vacuum-sealed.

At a temperature of 325 K, the potential between the heterostructure working electrode and Pt counter electrode was swept at a rate of approximately 1 mV s^{-1} in the presence of a small magnetic field, B, of 0.5 T. Simultaneously, the resistance of the device was monitored by applying a small AC (17.777 Hz) current (I_{ds}) of 0.1–1 μA between the source and drain terminals and measuring the four-terminal longitudinal voltage drop, V_{xx}, and Hall voltage, V_{xy}, using a lock-in amplifier (Stanford Research SR830). The resistances R_{xx} and R_{xy} were then obtained from the equations $R_{xx} = V_{xx}/I_{ds}$ and $R_{xy} = V_{xy}/I_{ds}$. The Hall carrier density, n_H, was then calculated from $n_H = B/(eR_{xy})$, where e is the elementary charge 1.602×10^{-19} C. The Hall mobility, μ_H, during the sweep was also determined from $\mu_H = (en_H\rho_{xx})^{-1}$, where the resistivity, ρ_{xx} is given by $\rho_{xx} = R_{xx}W/L$, where W represents the width of the conducting channel and L denotes the length of the channel between contacts. A voltmeter (Agilent 34401A Digital Multimeter) with a high internal impedance of >10 GΩ was used to measure the voltage between the heterostructure working electrode and the Pt pseudoreference electrode.

Upon reaching the desired potential, the temperature of the system was rapidly cooled to 200 K (10 K min^{-1}), thereby freezing the polymer electrolyte and effectively suspending any electrochemical reactions, after which additional magnetic field or temperature-dependent sweeps were conducted as desired. Further cooling to base temperature (1.8 K) was carried out at a slower rate of 2 K min^{-1}.

Provided that potential excursions did not exceed −6 V, we found transport behaviour to be stable to several cycles of these heterostructures.

Raman and photoluminescence spectroscopy studies. Raman and photoluminescence spectroscopy (Horiba Multiline LabRam Evolution) was conducted using 532-nm laser excitation at a power of 5–10 mW with 20-s acquisition times and four accumulations. For operando studies, the electrochemical cell or device was loaded in a glove-box environment into a cryostat (Cryo Industries of America, Inc.) with an optical window. The cryostat was then sealed, transferred out of the glove box and the measurement chamber evacuated to high vacuum for spectroelectrochemical measurements. The potential bias was swept at a rate of 2 mV s^{-1} to the desired potentials (0, −1, −2, −3, −4 and −5 V) and held at these potentials for the acquisition of Raman and photoluminescence spectra (around 10 min) before resuming the sweep. After intercalation, the heterostructure was deintercalated by sweeping the potential to +3 V and then back to 0 V. Removal of the electrolyte was accomplished by briefly washing in deionized water followed by isopropanol. Additional spectra were subsequently acquired in this state. The deintercalated heterostructure was then annealed at 300 °C for 1 h in high vacuum.

In the pristine heterostructure, the trigonal-prismatic coordination in H-MoS_2 resulted in only in-plane E_{2g}^1 and out-of-plane A_{1g} modes at about 383 cm^{-1} and 408 cm^{-1}. After a full cycle of intercalation and deintercalation, the E_{2g}^1 and A_{1g} peaks were diminished and new peaks were observed at 154, 184 and 226 cm^{-1}.

These low-wavenumber peaks grew in intensity with increasing numbers of MoS_2 layers—confirming their association with the dichalcogenide—and were still present, albeit slightly diminished, after annealing for 1 h at 300 °C. By contrast, the Raman peaks for the E_{2g}^1 and A_{1g} modes recovered spectral intensity after annealing. The 154 and 226 cm^{-1} peaks were attributed to the J_1 and J_2 modes of T′-MoS_2[23,24] and the 184 cm^{-1} feature was assigned to the J_1 mode of T-MoS_2[25]. The corresponding Raman spectrum peak of the J_2 mode for T-MoS_2 is expected[25] at around 203 cm^{-1} and therefore explains the low-wavenumber tail of the T′ J_2 peak observed in Fig. 2c. We did not observe the emergence of any Raman signatures for lithium polysulfides (746 cm^{-1})[11] during the entire intercalation–deintercalation processes, which suggests that the overall chemical integrity of MoS_2 remained intact upon lithiation, with a mixed phase of metastable T- and T′-MoS_2 persisting upon deintercalation, and partial recovery of H-MoS_2 after annealing.

Raman and photoluminescence spatial mapping was carried out ex situ (after removal of electrolyte) using 1.0-μm step sizes, 2-s acquisition times and two accumulations at each pixel or step point.

Low-temperature charge transport and magnetoresistance analysis. *SdH carrier densities.* SdH oscillations in $R_{xx}(B)$ arise because of the formation of Landau levels at high magnetic fields[26]. Plotting $R_{xx}(B)$ as a function of B^{-1} confirmed that these oscillations are periodic in B^{-1} with a frequency B_F. The associated carrier density of the 2DEG, n_{SdH}, could then be determined from the relation $n_{SdH} = \left(\frac{geB_F}{h}\right)$, where g is the Landau level degeneracy, e is the elementary charge and h is Planck's constant. For these electron-doped graphene or MoX_2 layers, it is reasonable to assume that $g = 4$. Spin–valley locking in the valence band of H-MoX_2 layers gives rise to degeneracies of $g = 2$, whereas the conduction band-edges are almost spin degenerate, leading to degeneracies closer to 4 for electron-doped H-MoS_2[18]. Theoretical studies to date do not reveal spin-split conduction bands in T- or T′-phases of MoS_2[32,33]. Regardless, the dependence of Hall and SdH carrier densities on the backgate voltage V_g provides additional validation for our assignment of the origin of SdH oscillations in the intercalated heterostructures. We found that, in the case of a structure-I stack consisting of a single graphene monolayer encapsulated by h-BN and biased up to $E = -5.5$ V for intercalation, n_{SdH} and n_H were about 2.6×10^{13} cm^{-2} at $V_g = 0$ V, changed together, and were effectively indistinguishable from each other for V_g values between −100 V and +100 V (Extended Data Fig. 7). This reveals SdH and Hall measurements dominated by a single band as expected. In the case of the h-BN-encapsulated MoS_2/graphene heterostructure (structure II) studied here, the graphene monolayer channel is positioned in closer proximity to the backgate, underneath the MoS_2 channel. The Landau fan diagram (Fig. 3c), in which R_{xx} is plotted as a function of both V_g and B, revealed that the SdH quantum oscillations are strongly dependent on V_g, pointing to the graphene as the origin of the magneto-oscillations. Were it the case that the MoS_2 layer served as the origin of the SdH oscillations, the SdH channel would be electrostatically screened by graphene and the associated density would therefore be independent of V_g. We found that n_{SdH} changes with V_g in a manner consistent with the capacitance of the SiO_2/Si backgate (Fig. 3d). Indeed, we estimated the backgate capacitance, $C = 1.2 \times 10^{-8}$ F cm^{-2}, using $\Delta n_H = CV_g/e$, the value of which is in good agreement with the thickness of SiO_2 and h-BN layers serving as the gate dielectric. Considering that n_H is the total density of the heterostructure that incorporates n_{SdH}, we deduced that the density in only one layer (corresponding to n_{SdH}) is dependent on V_g. This result reveals that the layer in closest proximity to the backgate (graphene) is responsible for SdH oscillations (lower density), and therefore enables us to determine the degree of charge transfer to the individual MoX_2 and graphene layers.

Effective mass determination, quantum scattering and mobilities. The effective mass, m^*, of the band giving rise to SdH oscillations was determined from the temperature dependence of the SdH amplitude, ΔR_{xx} (Fig. 4b), by fitting these data to the Lifshitz–Kosevich theory[27]:

$$\Delta R_{xx}(B,T) \propto \frac{\frac{\alpha T}{\Delta E_N(B)}}{\sinh\left(\frac{\alpha T}{\Delta E_N(B)}\right)} e^{\left(-\frac{\alpha T_D}{\Delta E_N(B)}\right)}$$

where B is the magnetic field position of the Nth minimum in R_{xx}, $\Delta E_N(B) = heB/2\pi m^*$ is the energy gap between the Nth and $(N+1)$th Landau levels (m^* is the effective mass, e is the elementary charge, and h is the Planck constant), $T_D = \frac{h}{4\pi^2\tau_q k_B}$ is the Dingle temperature (k_B is Boltzmann's constant, τ_q is the quantum lifetime of carriers, and $\alpha = 2\pi^2 k_B$ is the momentum space area including spin degeneracy. In our experiment, ΔE_N and T_D are the only two fitting parameters. The pre-exponential in this expression is the only temperature-dependent portion and permits the straightforward determination of m^* and τ_q. In the case of intercalated structure II (h-BN/MoS_2/graphene/h-BN), we determined $m^* = 0.11m_0$, and a T_D of 36.2 K, which indicates $\tau_q = 33.6$ fs and a mean free path, $l = \nu_f\tau_q$ (where ν_f is the Fermi velocity that is taken as 10^6 m s^{-1} for

graphene) of around 34 nm. We also determined the quantum mobility, $\mu_{q} = \frac{e\tau_{q}}{m^{*}} = 558 \, cm^{2} \, V^{-1} \, s^{-1}$ as compared to a Hall mobility μ_{Hall} of 270 cm^{2} V^{-1} s^{-1}. These values are compared to the parameters obtained for intercalated structure I (h-BN/graphene/h-BN) in Extended Data Table 1.

(Scanning) transmission electron microscopy. VdW heterostructures were fabricated as described above and finally transferred onto a 50-nm-thick holey amorphous silicon nitride membrane. Upon sweeping the potential, E, to the desired stage in the plot of R_{xx} against E, the potential was immediately returned to 0 V after which the electrolyte was removed by washing in distilled water followed by isopropanol. The delithiated heterostructure was then analysed by TEM. Abberation-corrected HAADF and bright-field STEM imaging as well as SAED were conducted on a Jeol ARM 200F equipped with a cold field-emission gun. STEM was operated at 80 kV with a probe convergence angle of 23 mrad. The inner collection semi angle for HAADF STEM imaging was 68 mrad. Bright-field and dark-field TEM imaging and SAED were performed on a Tecnai F20 operated at 120 kV. SAED data were acquired using a 300 nm aperture. Although STEM imaging is based on projected atomic structures, we still obtained atomic resolution images of monolayer MoS$_{2}$ from the heterostructures by exploiting Z (atomic number)-contrast in HAADF-STEM imaging and by using few-layer h-BN crystals. All STEM images shown in Fig. 5b, c represent the raw, unfiltered data. For the bright-field STEM image in Extended Data Fig. 11d, a Wiener filter[34] was applied to remove noise. Fast Fourier transforms of atomic-resolution images in specified regions (Fig. 5c), as well as the inverse fast-Fourier-transform analysis (Extended Data Fig. 11), uncovers local crystallinity with domain sizes of the order of 5–10 nm.

DFT computations. DFT computations were performed using the projector augmented wave (PAW) method[35] as implemented in the VASP code[36–39]. Van der Waals interactions were included using the zero damping DFT-D3 method of Grimme[40]. The heterobilayer graphene/MoS$_{2}$ system was modelled with a supercell consisting of a layer of 5×5 unit cells of fully relaxed graphene, a layer of 4×4 unit cells of MoS$_{2}$ uniformly compressed by 2.5% (in order to match the graphene lattice spacing), and over 17 Å of vacuum space between successive layers in the direction perpendicular to the layer plane. There are 98 total atoms in the bilayer supercell. All calculations were performed with an energy cut-off of 400 eV. A Γ-centred k-point mesh of $5 \times 5 \times 1$ was used for structural relaxations until all forces were smaller in magnitude than 0.01 eV (for 0 and 1 intercalated Li ions) or 0.05 eV (for 2 or more Li ions). The k-point mesh was increased to $11 \times 11 \times 1$ for electronic density of states and band structure computations. When relaxing the ions within the supercell, one Mo atom was held fixed as a reference point,

and the C atom directly above it was held fixed in the plane of the graphene layer to preserve the registration of the two layers, but was free to relax in the vertical direction. All other atoms were unconstrained. We determined the energetic stability of different intercalation states in various vdW heterostructures by calculating the binding (intercalation) energy per Li atom[28], E_{I} (Fig. 5d):

$$E_{I} = \frac{1}{n}[E(M, nLi) - E(M) - nE(Li)]$$

where n is the number of Li atoms intercalated, $E(M)$ is the energy of the empty structure M (that is, 0 Li added), $E(M, nLi)$ is the energy of the structure M with n Li atoms intercalated and $E(Li)$ is the energy of a Li atom in bulk lithium.

Data availability. The datasets generated and/or analysed during the current study are available from the corresponding author upon reasonable request.

30. Lee, G.-H. et al. Flexible and transparent MoS$_{2}$ field-effect transistors on hexagonal boron nitride-graphene heterostructures. *ACS Nano* **7**, 7931–7936 (2013).
31. Cui, X. et al. Multi-terminal transport measurements of MoS$_{2}$ using a van der Waals heterostructure device platform. *Nat. Nanotechnol.* **10**, 534–540 (2015).
32. Kan, M. et al. Structures and phase transition of a MoS$_{2}$ monolayer. *J. Phys. Chem. C* **118**, 1515–1522 (2014).
33. Ma, F. et al. Predicting a new phase (T″) of two-dimensional transition metal di-chalcogenides and strain-controlled topological phase transition. *Nanoscale* **8**, 4969–4975 (2016).
34. Kilaas, R. Optimal and near-optimal filters in high-resolution electron microscopy. *J. Microsc.* **190**, 45–51 (1998).
35. Kresse, G. & Joubert, D. From ultrasoft pseudopotentials to the projector augmented wave method. *Phys. Rev. B* **59**, 1758 (1999).
36. Kresse, G. & Hafner, J. Ab initio molecular dynamics for liquid metals. *Phys. Rev. B* **47**, 558–561 (1993).
37. Kresse, G. & Hafner, J. Ab initio molecular-dynamics simulation of the liquid-metal–amorphous-semiconductor transition in germanium. *Phys. Rev. B* **49**, 14251–14269 (1994).
38. Kresse, G. & Furthmüller, J. Efficiency of ab-initio total energy calculations for metals and semiconductors using a plane-wave basis set. *Comput. Mater. Sci.* **6**, 15–50 (1996).
39. Kresse, G. & Furthmüller, J. Efficient iterative schemes for ab initio total-energy calculations using a plane-wave basis set. *Phys. Rev. B* **54**, 11169–11186 (1996).
40. Grimme, S., Antony, J., Ehrlich, S. & Krieg, H. A consistent and accurate ab initio parametrization of density functional dispersion correction (DFT-D) for the 94 elements H-Pu. *J. Chem. Phys.* **132**, 154104 (2010).
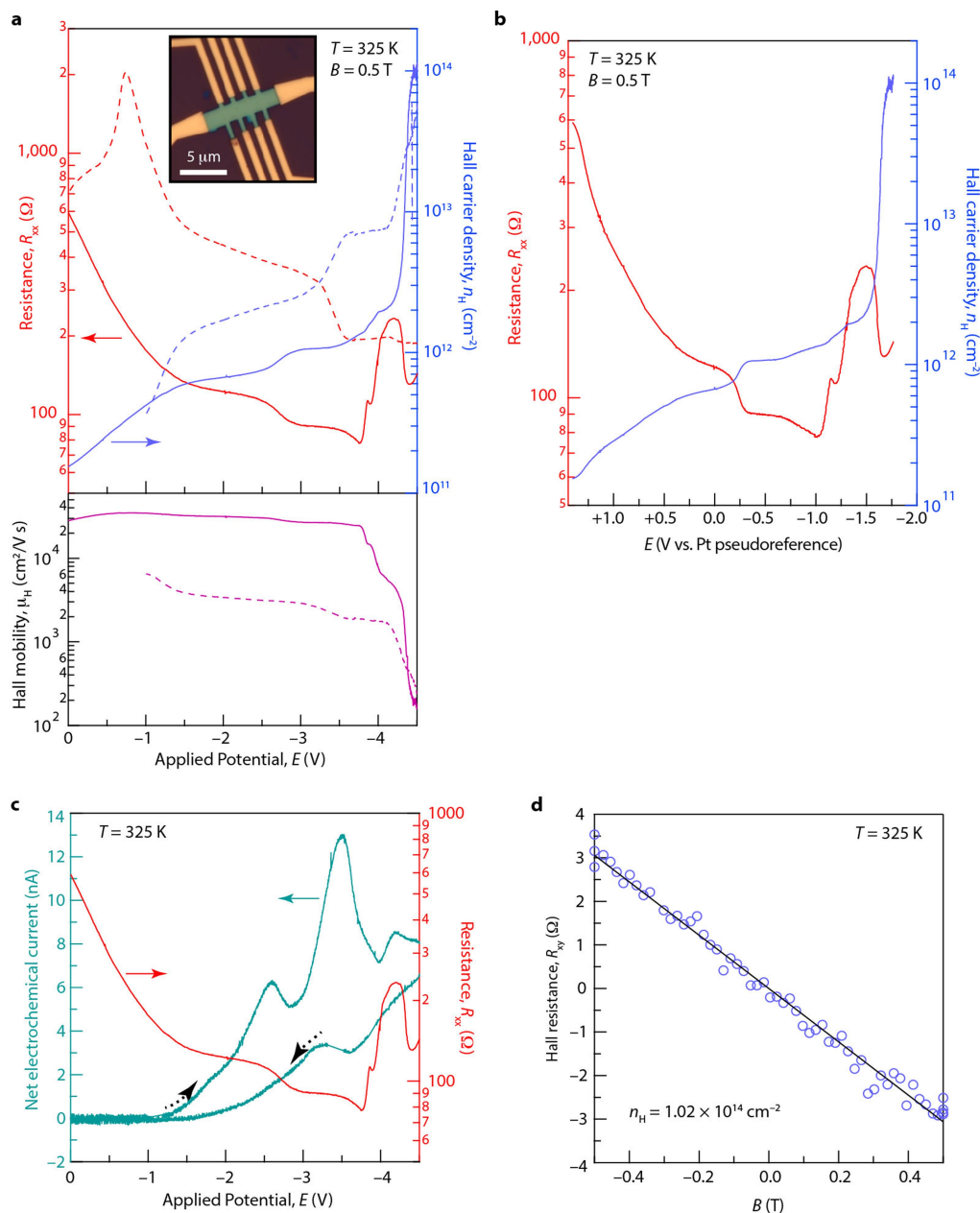
Extended Data Fig. 1 | Additional electrochemical and Hall data for the structure-II graphene/MoSe₂ stack. a, Forward (solid lines) and reverse (dashed lines) sweeps of four-probe resistance (red), Hall carrier density (blue), and Hall mobility (purple) as a function of potential at the heterostructure (versus the counter electrode/electrolyte gate—that is, in a two-electrode electrochemical configuration) in a LiTFSI/PEO electrolyte at 325 K in the presence of a magnetic field, $B = 0.5$ T. Inset, optical micrograph of heterostructure stack working electrode. **b,** Identical experiment to that in **a** with the resistance (red) and Hall

carrier density (blue) plotted as a function of the potential measured relative to a Pt pseudoreference electrode. **c,** Conventional cyclic-voltammetric electrochemical current response (green) overlaid with the resistance (red) over the course of the sweep, showing peaks that are difficult to assign directly to any specific reaction, probably incorporating side reactions at the Pt/electrolyte and Au/electrolyte interfaces. **d,** Hall resistance R_{xy} as a function of magnetic field at 325 K after intercalation ($E = -4.5$ V).
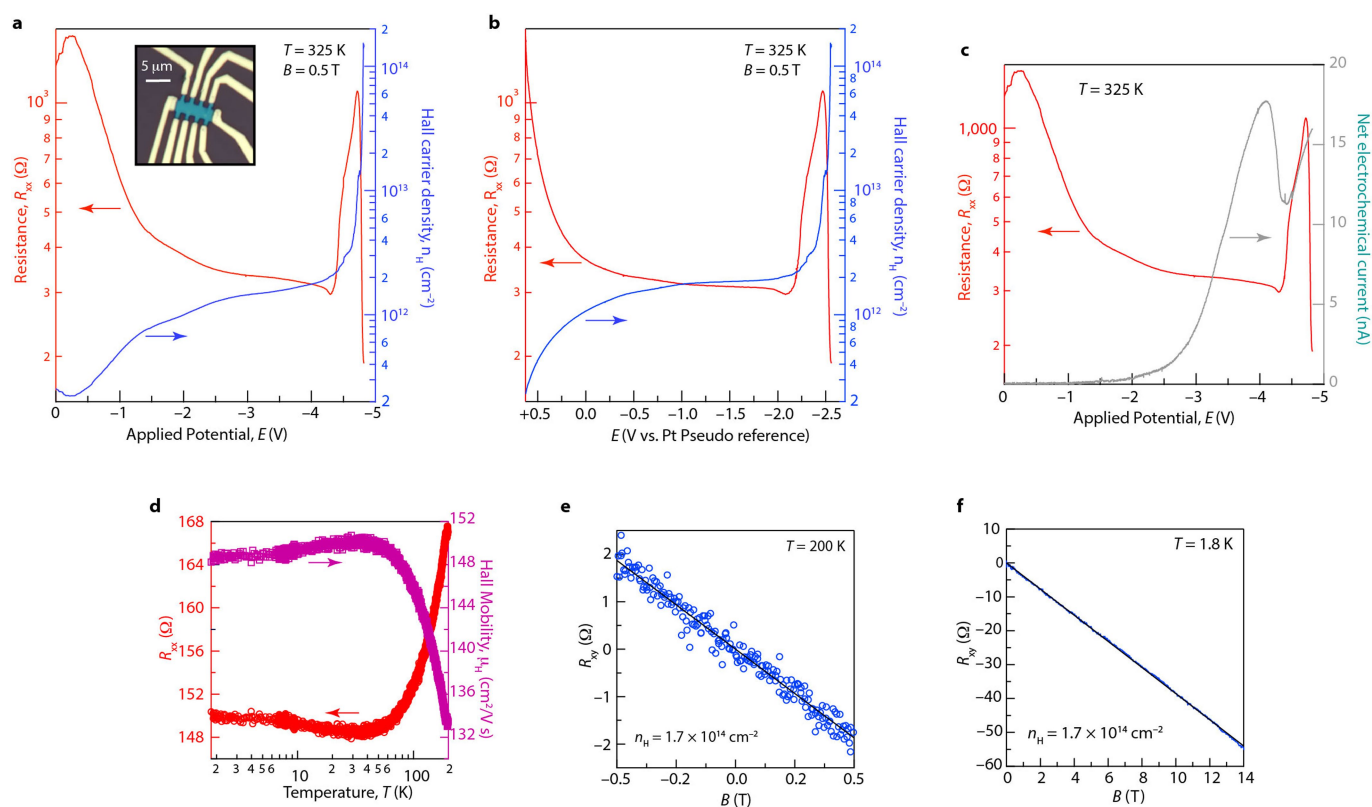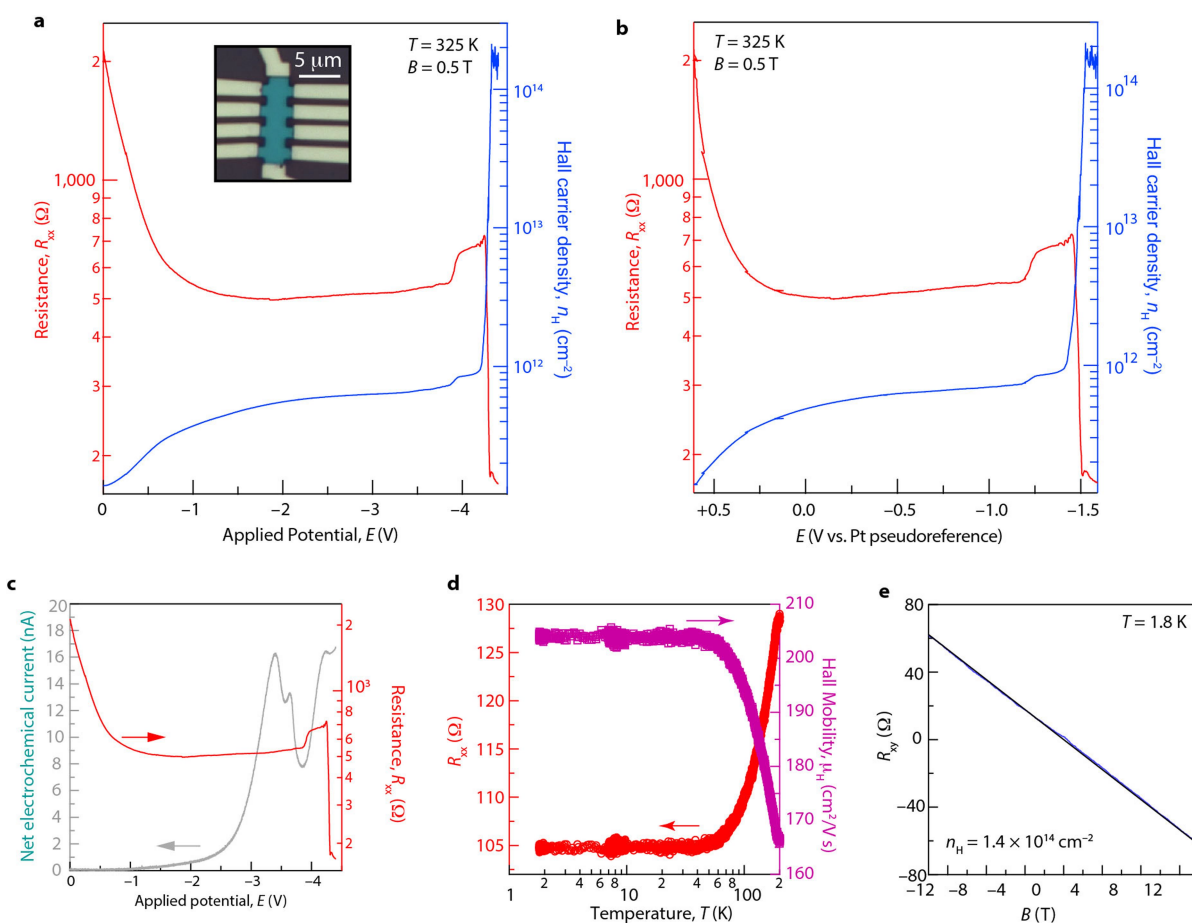
Extended Data Fig. 2 | Additional electrochemical and Hall data of the structure-II graphene/MoS$_2$ stack. a, **b**, Resistance (red) and Hall carrier density (blue) as a function of potential in a two-electrode (potential versus counter; **a**) and three-electrode (potential versus Pt pseudoreference; **b**) electrochemical configuration in a LiTFSI/PEO electrolyte at 325 K in the presence of a magnetic field, B, of 0.5 T. Inset, optical micrograph of heterostructure stack 'working electrode'.

c, Conventional cyclic-voltammetric electrochemical current response (grey) overlaid with the resistance (red) over the course of the sweep. **d**, Temperature dependence of resistance (red) and Hall mobility (purple) between 200 K and 1.8 K. **e**, Hall resistance, R_{xy}, as a function of magnetic field after cooling to 200 K immediately after the termination of a sweep to −4.8 V. **f**, Hall resistance R_{xy} as a function of magnetic field at 1.8 K.
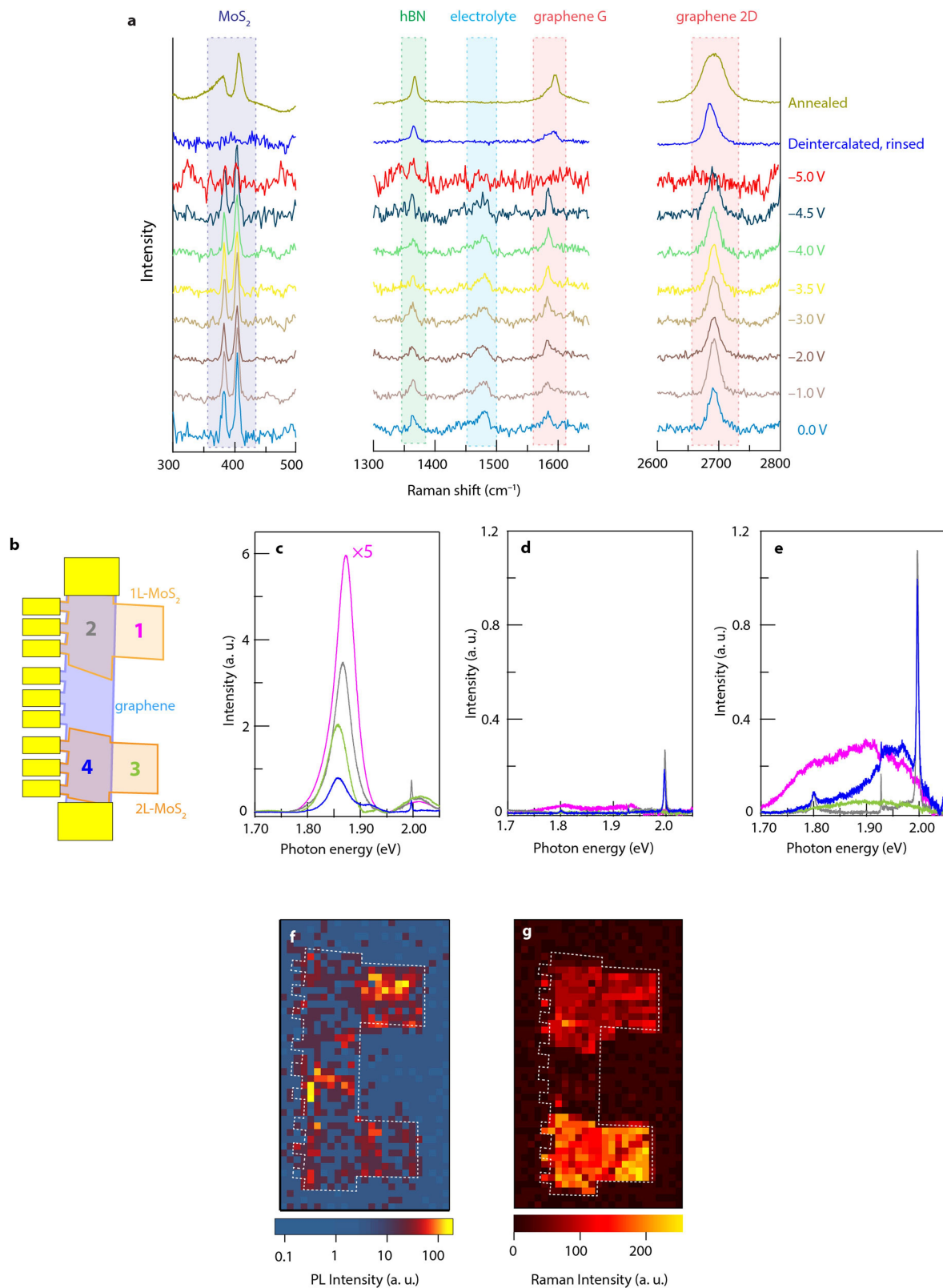
Extended Data Fig. 3 | Additional Raman and photoluminescence spectroscopy data. a, Raman spectra of an h-BN/graphene/MoS$_2$ structure-II device (identical device to that in Fig. 2b) over the course of electrochemical intercalation, showing the disappearance of spectral features of graphene and MoS$_2$ after full intercalation at -5.0 V, consistent with Pauli blocking in addition to the 2H→1T′ phase transition of MoS$_2$. Deintercalation restores graphene peaks, and annealing at 300 °C for 1 h restores the 2H-MoS$_2$ peaks. Each spectrum is offset for clarity. **b–g**, Schematic diagram (**b**), photoluminescence spectra (**c–e**), photoluminescence map (**f**) and Raman map over the 350–450 cm^{-1}

range (**g**) of an h-BN-encapsulated multi-structure device (identical device to that in Fig. 2d–g) that consists of a graphene monolayer straddling a monolayer MoS$_2$ crystal at one end and a bilayer MoS$_2$ crystal at the other. Data were acquired on the pristine stack before intercalation (**c**), after deintercalation followed by removal of electrolyte (**d**) and after subsequent annealing at 300 °C for 1 h (**e–g**). The sharp peak at almost 2 eV is the graphene two-dimensional (Raman scattering) peak. Photoluminescence spatial maps in the pristine state and after deintercalation are presented in Fig. 2e, f and the map of the spatial intensity of the J_2 Raman peak of the T′ phase (around 226 cm^{-1}) after annealing is shown in Fig. 2g.

Extended Data Fig. 4 | Electrochemical and Hall data of structure III graphene/MoS$_2$ stack. a, Resistance (red) and Hall carrier density (blue) as a function of potential in a two-electrode (potential versus counter; **a**) and three-electrode (potential versus Pt pseudoreference; **b**) electrochemical configuration in a LiTFSI/PEO electrolyte at 325 K in the presence of a magnetic field B of 0.5 T. Inset, optical micrograph of heterostructure stack 'working electrode'. **c**, Conventional cyclic-voltammetric electrochemical current response (grey) overlaid with the resistance (red) over the course of the sweep. **d**, Temperature dependence of resistance (red) and Hall mobility (purple) between 200 K and 1.8 K. **e**, Hall resistance R_{xy} as a function of magnetic field at 1.8 K. This device shows a carrier density of 1.4×10^{14} cm^{-2}. Maximum carrier density observed for structure-III devices is 1.9×10^{14} cm^{-2}.
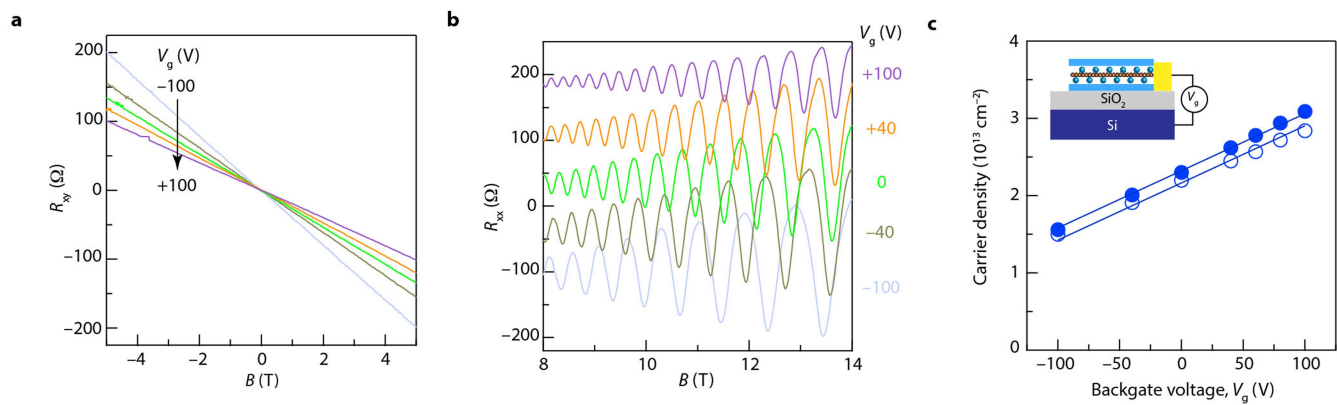
Extended Data Fig. 5 | Dependence of carrier densities of intercalated structure I on backgate voltage. a, **b**, Hall resistance (**a**) and magnetoresistance, (**b**; individually offset for clarity), as a function of magnetic field strength, B, in the case of a structure-I device with varying backgate voltage, V_g. **c**, Dependence of change in Hall (filled circles) and SdH (open circles) carrier densities on V_g. Solid lines represent fits that assume a Si backgate capacitance of 1.2×10^{-8} F cm^{-2}.
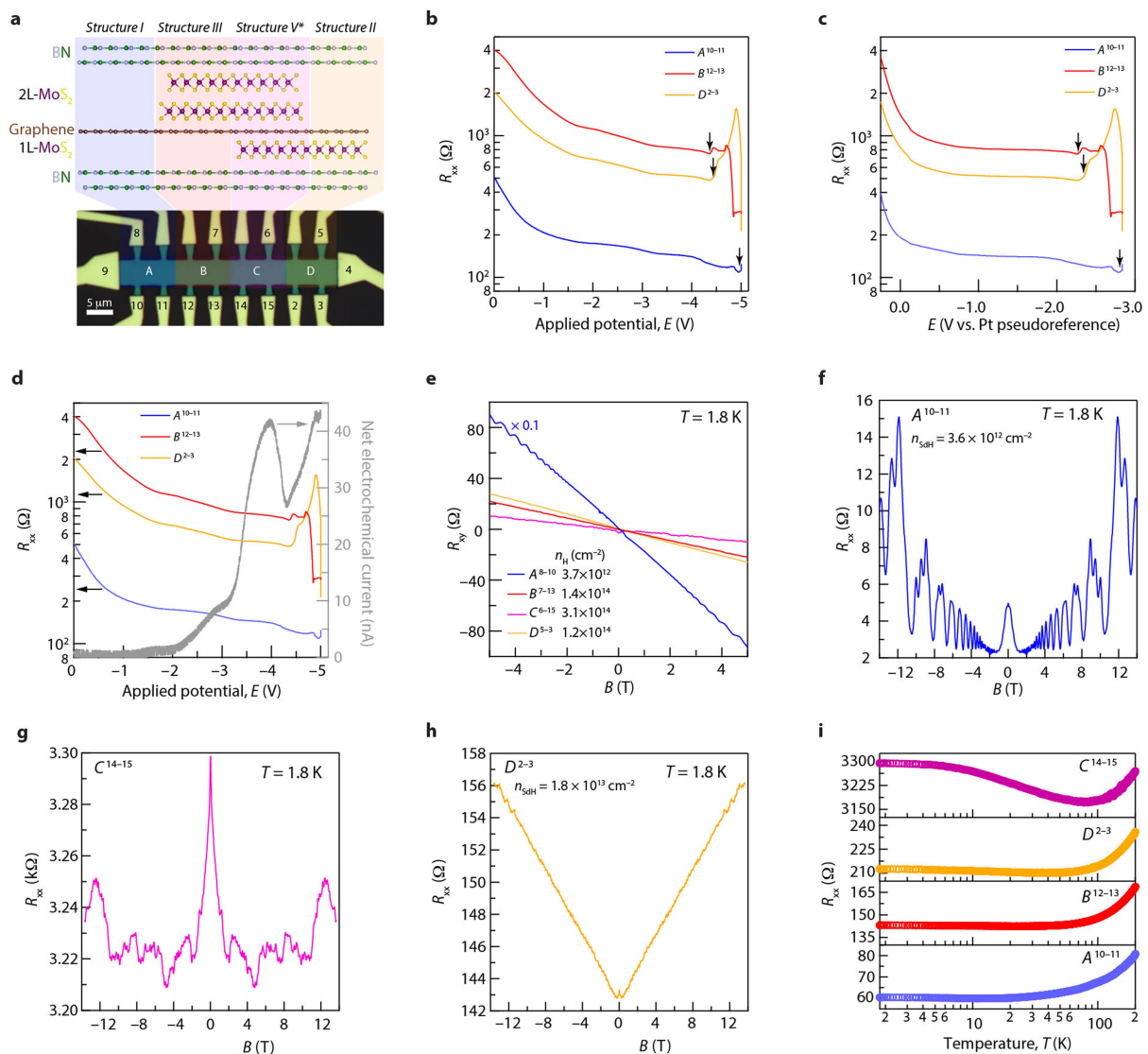
Extended Data Fig. 6 | Additional data on multi-structure-device 1.
a, Optical micrograph (false colour) of a device consisting of several h-BN-encapsulated graphene/MoS₂ heterostructure types (depicted in the associated illustration) arrayed along a single graphene monolayer (identical device to that in Fig. 4b). **b, c**, Zonal resistances as a function of potential in a two-electrode (potential versus counter; **b**) and three-electrode (potential versus Pt pseudoreference; **c**) electrochemical configuration. Intercalation (indicated by the arrows) initiates at potentials approximately 0.6 V more positive at zones B (structure III) and D (structure II) than at zone A (structure I). **d**, Conventional cyclic-voltammetric electrochemical current response (grey) of the entire device overlaid with the resistances of the various device regions over the course of the sweep. Cyclic voltammetry cannot distinguish between the intercalation of graphene/MoS₂ and graphene/h-BN regions in this device. **e**, Hall resistance R_{xy} as a function of magnetic field at 1.8 K for the different regions of the device after electrochemical polarization up to −5.0 V, displaying the resulting Hall carrier densities obtained. **f–h**, Magnetoresistance data at 1.8 K for zones A (**f**), C (**g**) and D (**h**), showing associated SdH carrier densities n_{SdH} extracted from the periodicities of oscillations in B^{-1}. **i**, Temperature dependence of resistance for the various device regions between 200 K and 1.8 K during warming.
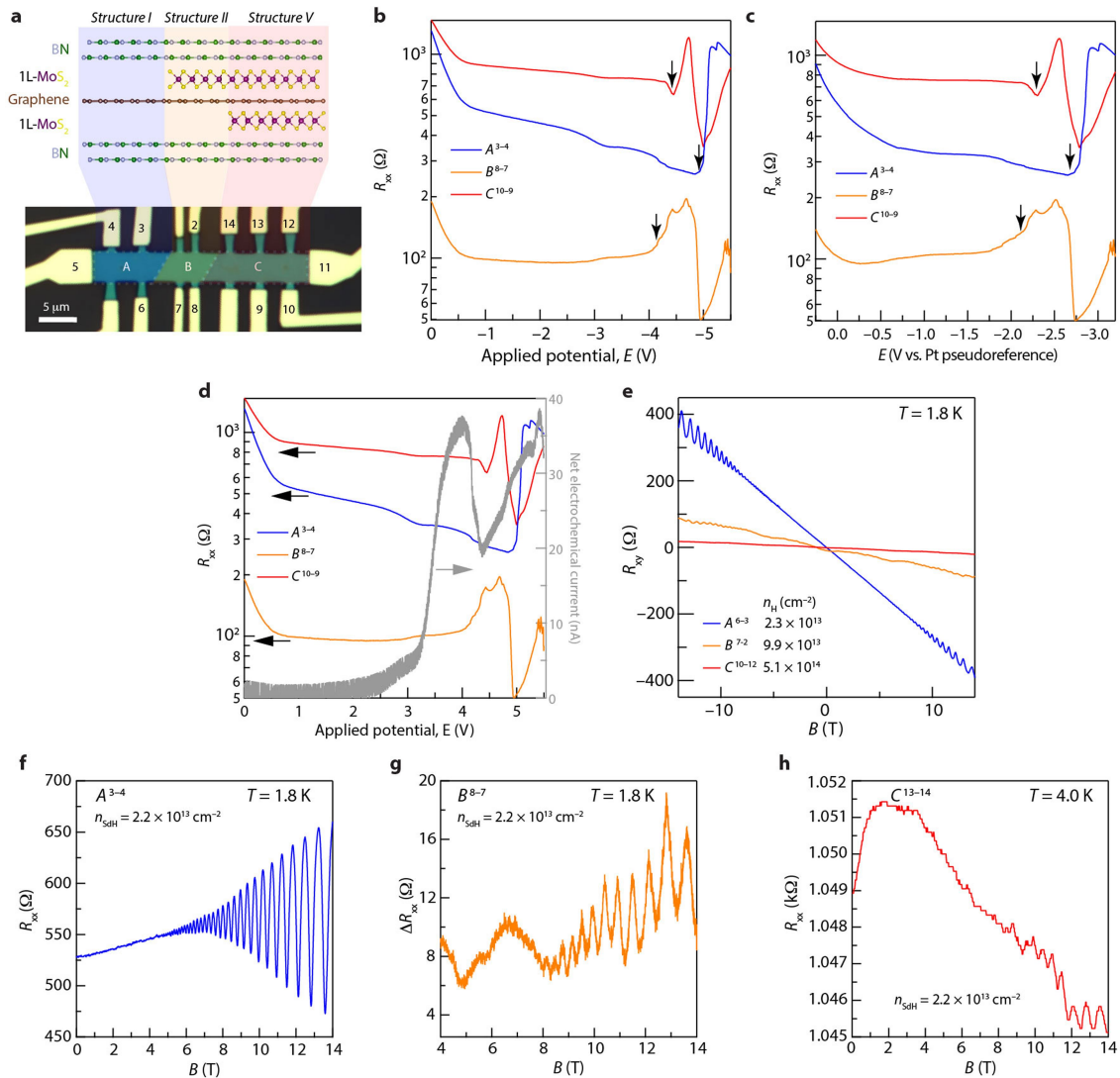
**Extended Data Fig. 7 | Additional data on multi-structure-device 2.**
a, Optical micrograph (false colour) of a device consisting of multiple h-BN-encapsulated graphene/MoS$_2$ heterostructure types (depicted in the associated illustration) arrayed along a single graphene monolayer. **b, c**, Zonal resistances as a function of potential in a two-electrode (potential versus counter; **b**) and three-electrode (potential versus Pt pseudoreference; **c**) electrochemical configuration. Intercalation (indicated by the arrows) initiates at potentials approximately 0.7 V more positive at zones B (structure II) and C (structure V) than at zone A (structure I). **d**, Conventional cyclic-voltammetric electrochemical current response (grey) of the entire device overlaid with the resistances of the various device regions over the course of the sweep. Cyclic voltammetry cannot distinguish between the intercalation of graphene/MoS$_2$ and graphene/h-BN regions in this device. **e**, Hall resistance R_{xy} as a function of magnetic field at 1.8 K for the different regions of the device after electrochemical polarization up to −5.5 V, displaying the resulting Hall carrier densities obtained. **f–h**, Magnetoresistance data at 1.8 K for regions A (**f**), B (**g**), and C (**h**) that reveal associated SdH carrier densities, n_{SdH} from the periodicities of oscillations.
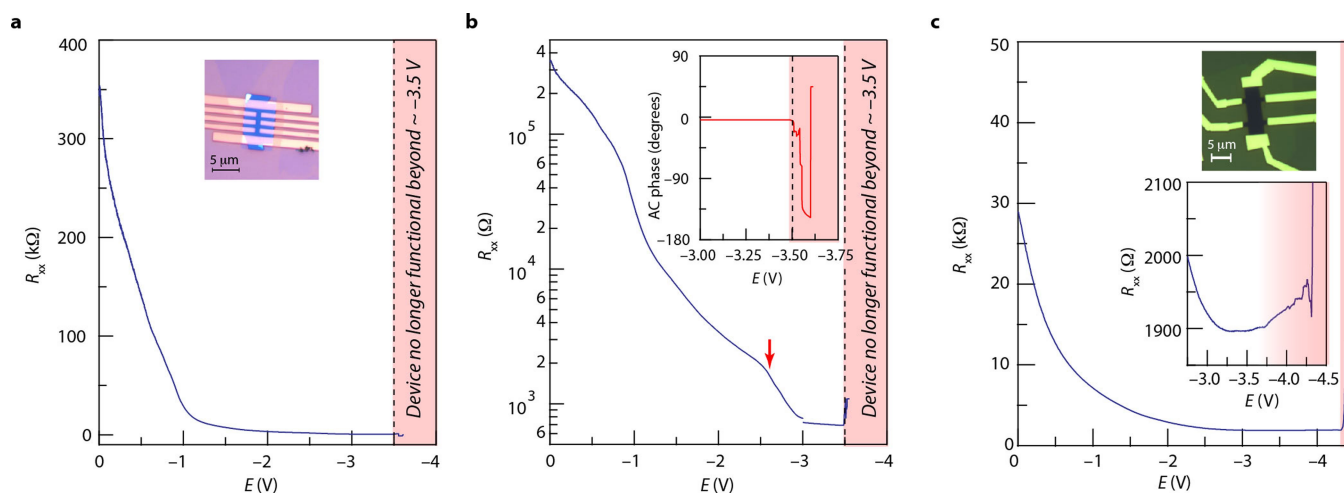
Extended Data Fig. 8 | Electrochemical gating of non-encapsulated few-layer (4–5 layers) MoX$_2$. a, b, Four-terminal resistance, R_{xx}, of a few-layer MoSe$_2$ crystal on a linear (**a**) and a logarithmic (**b**) scale, during electrochemical gating in an electrolyte comprising LiTFSI dissolved in diethylmethyl(2-methoxyethyl)ammonium TFSI (DEME-TFSI). Intercalation takes place between −2.5 V and −3 V (red arrow) and the device loses electrical contact (demonstrated by the disruption in the phase of the lock-in amplifier (inset)) beyond −3 V. **c,** Four-terminal resistance, R_{xx}, of a few-layer MoS$_2$ device during electrochemical gating in a LiTFSI/PEO electrolyte. As in **a**, the resistance of this device begins to increase at around −3.5 V and is completely insulating beyond −4.25 V, which is indicative of conversion to lithium polysulfide.
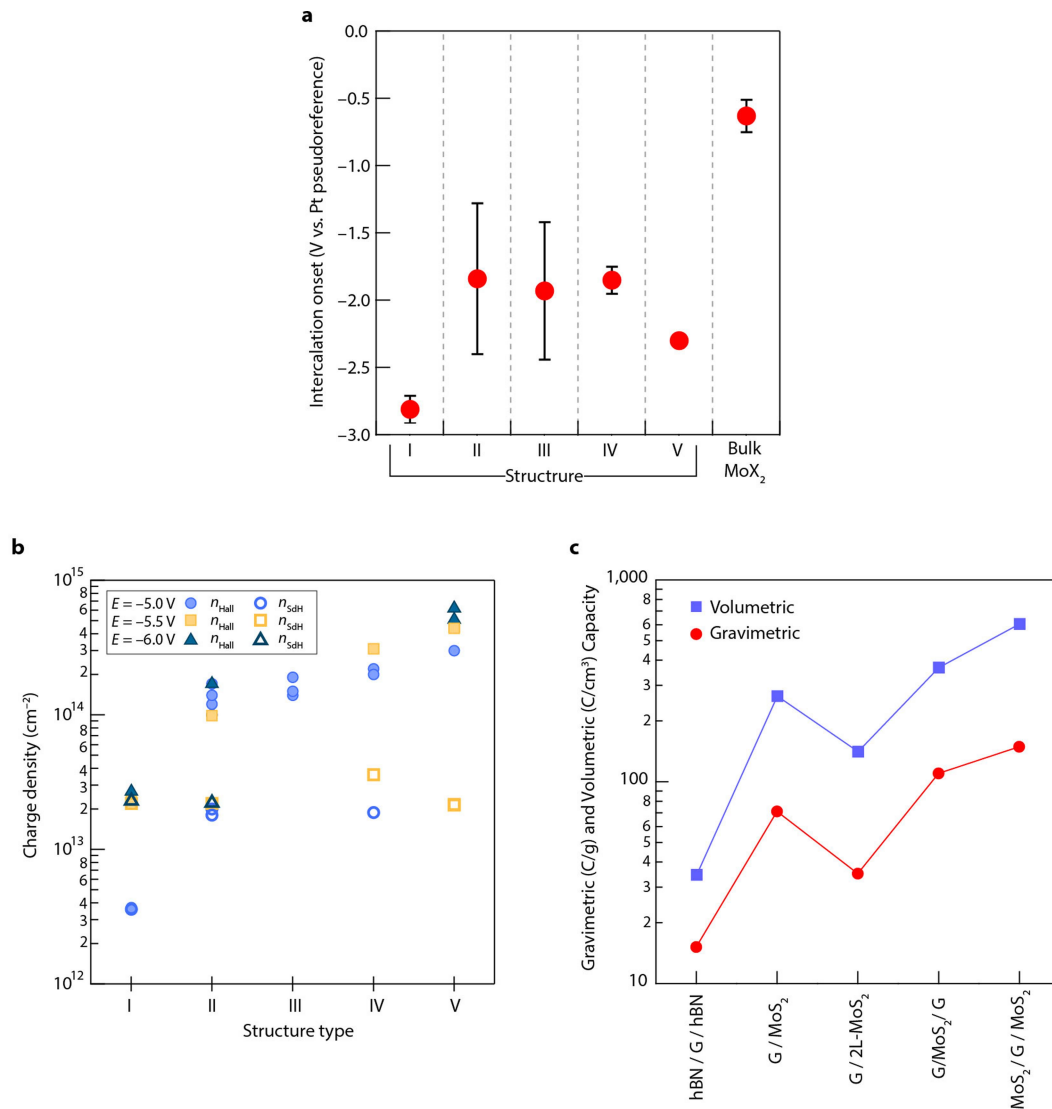
Extended Data Fig. 9 | Onset potentials and charge capacities of various heterostructures. a, Intercalation onset potentials (versus Pt pseudoreference electrode) for different vdW heterostructure types as well as few-layer MoX_2. Error bars represent standard deviations (from left to right, $n = 3, 5, 4, 2, 1, 3$) of measurements from multiple devices or distinct contact pairs. **b**, Carrier densities attained after intercalation of various h-BN/graphene/MoX_2 heterostructures. Circles, squares and triangles represent densities reached after intercalation at up to −5, −5.5, and −6 V, respectively. Filled symbols designate densities determined from Hall data (revealing approximate MoX_2 carrier densities, except in the case of structure I), whereas hollow symbols represent densities extracted from SdH oscillations (revealing graphene carrier densities). **c**, Average capacity values from devices in **b**, expressed in units of C g^{-1} (gravimetric capacity) and (C cm^{-3}) volumetric capacity.

TEM Device 1

a

b

4 µm

c

$\{10\bar{1}0\}$

TEM Device 2

d

e

1 µm

f

$\{10\bar{1}0\}$
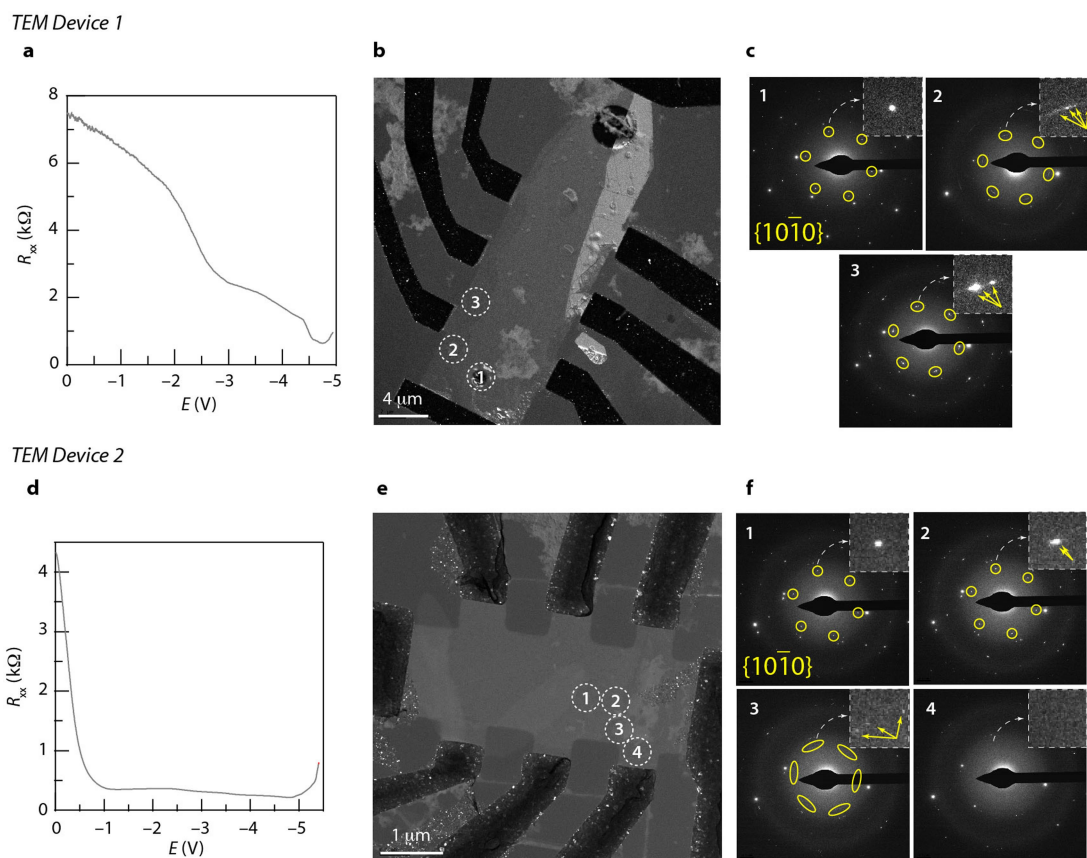
Extended Data Fig. 10 | Transmission electron microscopy data of incompletely intercalated structure-II devices. a, Resistance, R_{xx}, as a function of applied potential, E, of an h-BN/MoS$_2$/graphene vdW heterostructure fabricated onto a 50 nm holey amorphous silicon nitride membrane. The electrochemical reaction is suspended as the increase in R_{xx} is commencing by immediately sweeping the potential back to 0 V. **b**, $g_{MoS_2} = 11\bar{2}0$ dark-field TEM image of the device after removal of the electrolyte. **c**, SAED patterns acquired from the regions designated 1, 2, and 3 in **b**. SAED data reveal a pristine MoS$_2$ structure in region 1, but splitting of the Bragg spots (insets) at the edges of the heterostructure (regions 2 and 3) indicative of the formation of two or more domains. **d**, Resistance, R_{xx}, as a function of applied potential, E, of an h-BN/MoS$_2$/

graphene/h-BN vdW heterostructure. The electrochemical reaction is suspended as R_{xx} approaches a maximum by immediately sweeping the potential back to 0 V. **e**, $g_{MoS_2} = 11\bar{2}0$ dark-field TEM image of the device after removal of the electrolyte. **f**, SAED patterns of the regions designated 1, 2, 3, and 4 in **e**. SAED data reveal a pristine MoS$_2$ structure in region 1, but strong splitting of the Bragg spots (insets) towards the edge of the heterostructure (region 3) indicative of the formation of several domains. In region 4, the diffuse scattering from the underlying amorphous silicon nitride membrane obscures any diffraction features from the MoS$_2$, which in that region must be considerably disordered with any domain sizes ≪300 nm (the aperture size).

TEM Device 3
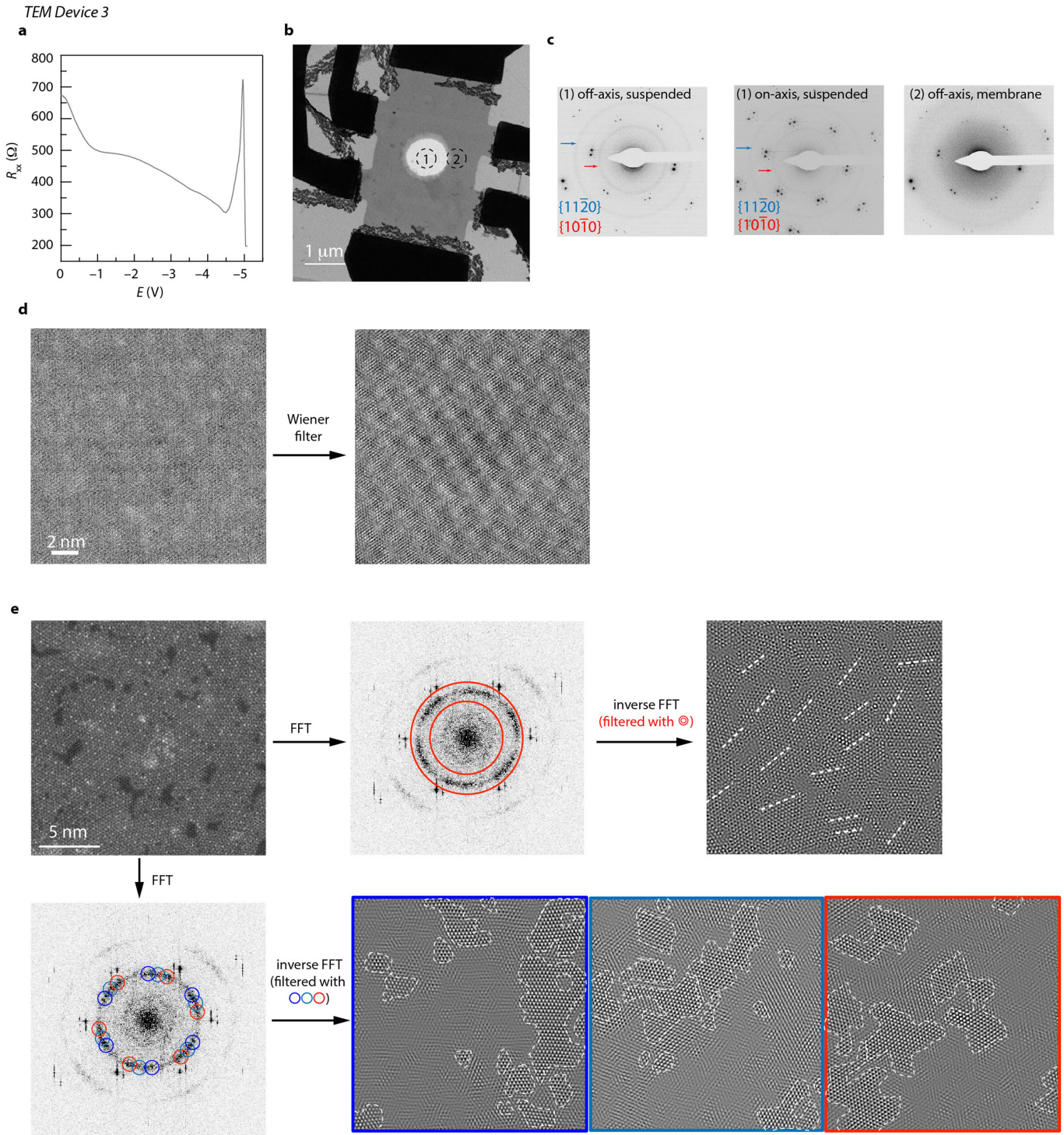
Extended Data Fig. 11 | (Scanning) transmission electron microscopy data of the fully intercalated structure-II device. a, Resistance, R_{xx}, as a function of applied potential, E, of an h-BN/MoS$_2$/graphene/h-BN vdW heterostructure fabricated onto a 50 nm holey silicon nitride membrane. The potential is reversed to 0 V after R_{xx} returns to a minimum (full intercalation) at around −5 V. **b**, Bright-field TEM image of the device after removal of the electrolyte. **c**, SAED patterns of the regions designated 1 and 2 in **b** in both the [0001] zone-axis (beam perpendicular to the plane of the heterostructure; middle panel) and off-zone-axis (sample tilted) conditions (left and right panels). The off-zone axis condition permits the minimization of double-diffraction phenomena associated primarily with the top and bottom h-BN flakes. SAED data at the suspended (no amorphous silicon nitride) window reveal two rings associated with

the MoS$_2$ layer, indicating considerable disorder in the x–y plane with a domain size ≪300 nm (the aperture size). SAED data acquired over the membrane (region 2) cannot resolve these MoS$_2$ diffraction features owing to the diffuse scattering from the amorphous silicon nitride membrane in that region. **d**, Aberration-corrected bright-field STEM image of the heterostructure (left, raw data; right, filtered data), which is dominated by the h-BN in the structure. The bright periodic patches arise from the moiré pattern of the two h-BN crystals. **e**, Aberration-corrected HAADF STEM image of the device showing the nanostructure of the MoS$_2$ layer after one cycle. Filtered inverse fast Fourier transform (FFT) data resolve x–y rotational disorder in the MoS$_2$ atomic chains (top right, white dashed lines, revealing the approximate domain sizes as 5–10 nm (bottom).
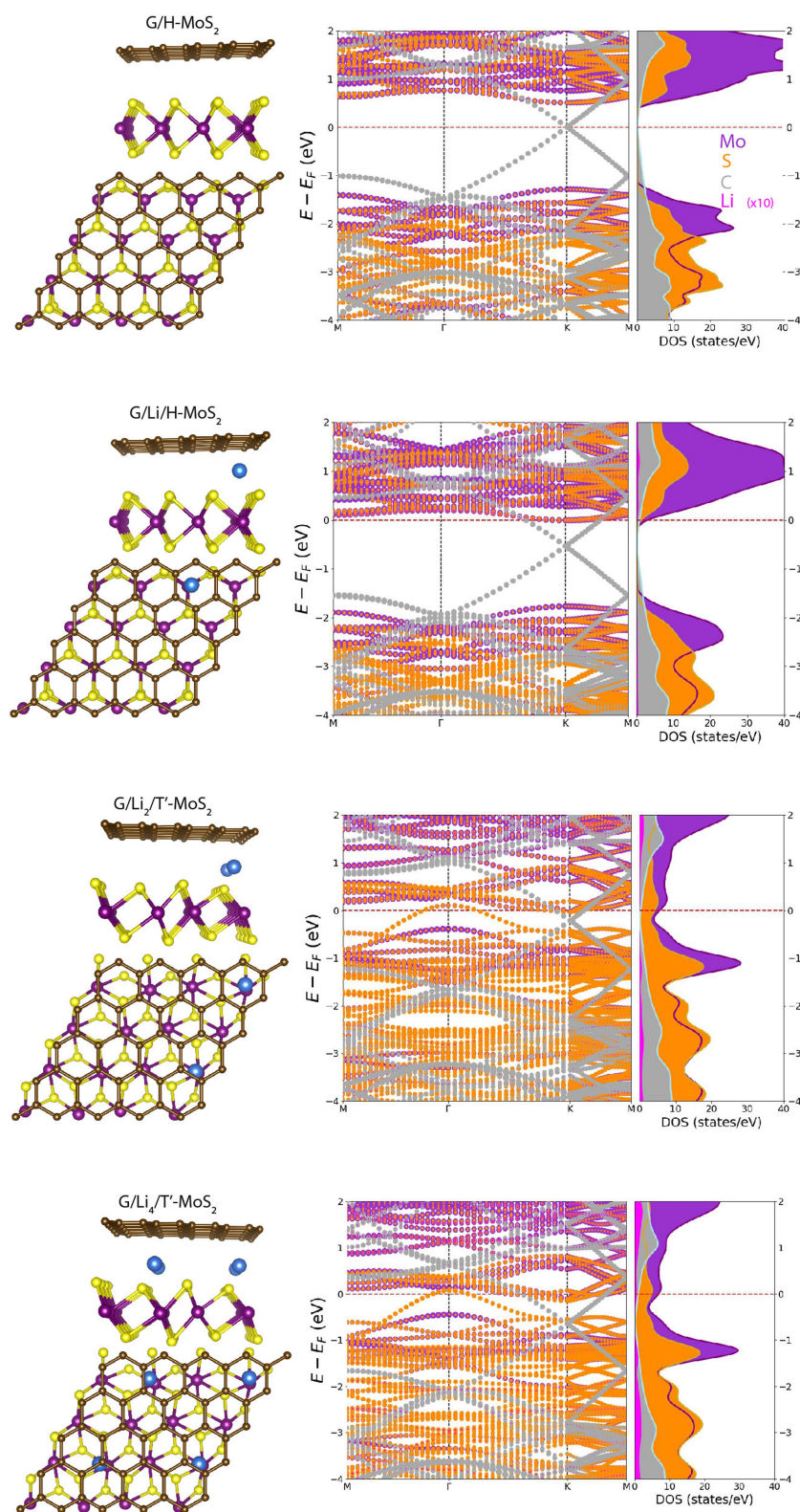
Extended Data Fig. 12 | DFT-computed electronic structures of graphene/MoS$_2$ heterobilayers over the course of Li intercalation. Relaxed geometries (left), band structures (middle), and density-of-states plots (right) for graphene/MoS$_2$ structures as Li atoms are incrementally added (top to bottom) and the phase of MoS$_2$ is changed from H to T'. The reason for the large carrier density in MoS$_2$ compared with that in graphene upon intercalation is evident from the relative density of states associated with MoS$_2$ compared to that of graphene.

Extended Data Table 1 | Charge transport parameters

Parameter	Structure **I** Intercalated ($E = -5.5$ V) hBN/G/hBN	Structure **II** Intercalated ($E = -5$ V) hBN/MoS$_2$/G/hBN
n_H	2.3×10^{13} cm^{-2}	1×10^{14} cm^{-2}
n_{SdH}	2.2×10^{13} cm^{-2}	2.0×10^{13} cm^{-2}
m^*	$0.099 m_0$	$0.11 m_0$
T_D	30.5 K	36.2 K
τ_q	39.9 fs	33.6 fs
l	40 nm	34 nm
μ_q	712 cm^{2}V^{-1}s^{-1}	557 cm^{2}V^{-1}s^{-1}
μ_H	462 cm^{2}V^{-1}s^{-1}	270 cm^{2}V^{-1}s^{-1}

Comparison of transport parameters for two classes of intercalated heterostructures. The relative similarity in quantum scattering time and mean free compound support the idea that SdH oscillations observed for intercalated structure II arise from the graphene sublayer.